

Silicon Photomultiplier Classification of the Pre-Production GCT Camera of CTA

Silicon Photomultiplier Klassifikation der Pre-Production GCT Kamera von CTA

Master-Thesis von Ben Gebhardt aus Heidelberg

Tag der Einreichung:

1. Gutachten: Dr. Richard White (MPIK)
2. Gutachten: Prof. Jim Hinton (MPIK)
3. Gutachten: Prof. Tetyana Galatyuk (TU DA)



TECHNISCHE
UNIVERSITÄT
DARMSTADT

Fachbereich Physik
Max Planck Institut für Kernphysik Heidelberg

Silicon Photomultiplier Classification of the Pre-Production GCT Camera of CTA
Silicon Photomultiplier Klassifikation der Pre-Production GCT Kamera von CTA

Vorgelegte Master-Thesis von Ben Gebhardt aus Heidelberg

1. Gutachten: Dr. Richard White (MPIK)
2. Gutachten: Prof. Jim Hinton (MPIK)
3. Gutachten: Prof. Tetyana Galatyuk (TU DA)

Tag der Einreichung:

Abstract

whats this about



Abstract

worum es geht



Contents

1	Cosmic Radiation	5
1.1	Air shower induced Cherenkov Radiation	7
2	Imaging Atmospheric Cherenkov Telescopes	9
2.1	Cherenkov Telescope Array	9
2.2	GCT	10
2.3	CHEC-S	11
2.4	SiPM requirements for CTA	11
3	Silicon Photomultipliers	13
3.1	Gain of a Silicon Photomultiplier	15
3.2	Thermally induced dark counts	16
3.3	Avalanche-induced secondary effects	17
3.4	OCT dependency on cellsize	18
3.5	Photon Detection Efficiency	18
4	Experimental Setup	21
5	Data Analysis	23
5.1	Tracefile Conversion	23
5.2	Pedestal Subtraction	24
5.3	Peak Detection	25
5.4	Gain Extraction	26
5.5	Data Challenges	27
6	Results	30
6.1	SiPM devices for CTA	30
6.2	Hamamatsu S12642-1616PA-50 50 μ m 3mm	32
6.3	Hamamatsu LCT5 50 μ m 6mm	37
6.4	Hamamatsu LCT5 75 μ m 7mm	41
6.5	Hamamatsu IVR 50 μ m 6mm	44
6.6	SensL FJ60035 6mm 35 μ m	47
7	Comparison	49
7.1	Dark Count Rate	49

7.2	Optical Cross Talk	50
7.3	Photon Detection Efficiency	52
7.4	Point of Operation Comparison	53
8	further analysis	54
8.1	Dark Count Rate recalibration with multi incident probability	54
8.2	Prompt and delayed cross talk ratio	54
9	Conclusion and Outlook	54
10	Glossary	55
11	Bibliography	56
12	Appendix	57

1 Cosmic Radiation

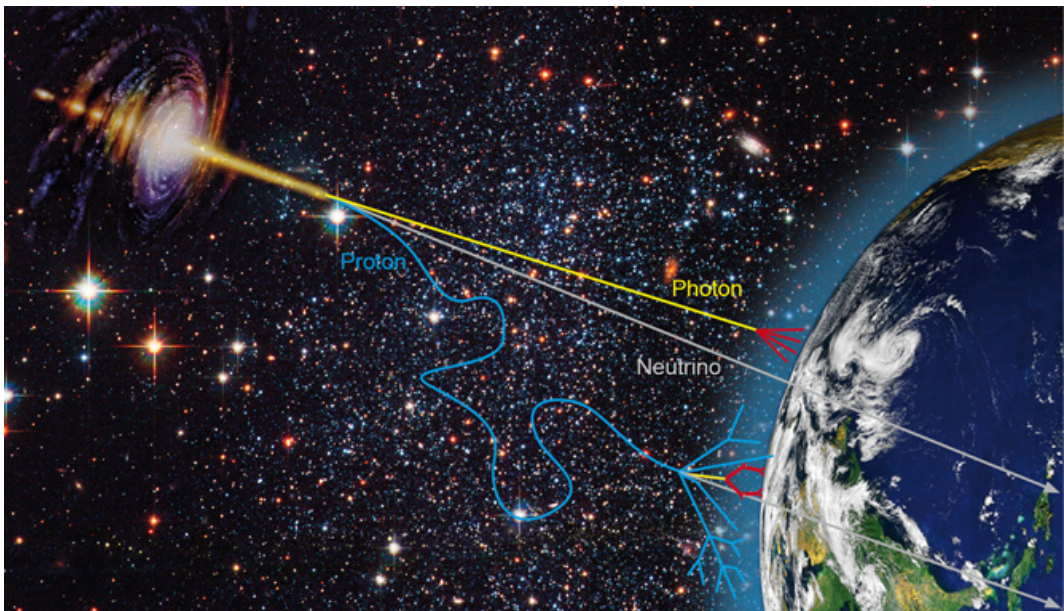


Figure 1: Gamma Radiation photons(yellow) and scattered cosmic ray protons(blue) from an astrophysical source arriving on earth. Neutrinos(grey) mostly do not interact.

Cosmic rays consist of a single particle with energies from 10^{10} to 10^{20} eV, the most energetic laboratory based accelerators operate in the 10^{12} eV energy range. The term cosmic rays describes charged particles hitting the earth's atmosphere. They were discovered by V.F. Hess in 1912 during the famous balloon flight experiments. He aimed to measure the conductivity of air, that until then, was believed to be an insulator resulting in some problems regarding the discharge of an electrically charged body, no matter how well it was isolated from the ground. Hess found the air's conductivity to increase with higher altitude, concluding the presence of a large amount of ionizing radiation above the atmosphere. Cosmic rays do not include those low energy particles originating from our sun. With a particle energy up to 1keV, those are referred to as solar wind, which means, by definition, cosmic rays arrive on Earth from outside our solar system. They consist of 87% protons, 12% α -particles , 1% heavier nuclei and some electrons.



Figure 2: FermiLAT

Cosmic Ray origin ? , energy spectrum? knee, ankle, power law?

High energy cosmic rays hitting Earth are very rare, averaging to one per year in an area of one square kilometer. Except at very high energies ($>10^{18}$ eV) cosmic rays will not reach earth directly and can not be observed to pinpoint their source. Traveling through the interstellar medium, they get scattered by the interstellar magnetic fields, the cosmic microwave background and other hindrances and therefore have lost all directional information. However, directly observable cosmic rays, for example at the Pierre-Auger Observatory, provide an insight into cosmic particle accelerators and their role in galactic discs.[3]

This means we have to observe high energy cosmic rays using a detour: Gamma radiation.

Gamma radiation cannot be generated by thermal emission of hot stellar objects, the only event with a high enough temperature to produce thermal radiation in the range of GeV and TeV gamma radiation would be the big bang, there is and has been nothing else in the known universe. So, if thermal radiation reflects the temperature of the emitting body, what do gamma rays tell us?

Gamma radiation probe a non-thermal universe. In this you need other mechanisms to concentrate large amounts of energy into a single quantum. But what are those?

There are many diverse mechanisms of emitting gamma radiation. Gamma rays are generated by high relativistic particles, in a first step for example: accelerated by the shockwave of a supernova explosion. Those cosmic rays then collide with ambient gas, interact with photons or magnetic fields, by inverse compton scattering, emitting high energy photons.

One such supernova remnant and also the most famous, while also being the, to date strongest in energy is the Crab Pulsar. The Neutron Star located inside the Crab Nebula is the remnant of Supernova 1054 and steadily emits gamma radiation energies up to 80TeV. The source of the gamma radiation here is the so called Pulsar Wind Nebula. It is composed of highly relativistic charged particles from the pulsars giant rotating magnetic field interacting with the expanding Supernova remnant via inverse compton scattering. Supernova shockwaves themselves can also drive atomic nuclei to high energies which in turn generate observable gamma-rays. Additionally, binary systems consisting of a black hole or pulsar orbiting a massive star can emit a flow of high-energy particles with varying intensity, based on the elliptical orbit, where particle acceleration conditions vary.

So just like thermal radiation reflects the temperature of the emitting object, the flux and energy spectrum of the gamma rays reflect the flux and spectrum of the high energy parti-

cles. So they can be used to trace these cosmic rays and electrons in distant regions of our own galaxy or even beyond.

One surprise was the discovery of so called "dark sources", objects emitting very-high-energy (VHE) gamma-rays, but have no counterpart in other wavelengths, meaning those objects might only be observable through gamma-rays. In extragalactic regions, gamma rays provide information on active galaxies, where a constant stream of gas feeds a supermassive black hole at the center, releasing enormous amounts of energy. From there, gamma rays are believed to be emitted, giving insight into one of the most violent but to date poorly understood environments in our universe. Even higher energy gamma rays could also be the product of decays of heavy particles, like dark matter or cosmic strings. They therefore also provide a window to the discovery of dark matter.

Gamma Radiation carries unique information about the most energetic phenomena in our universe. The only problem is, our atmosphere is opaque for gamma radiation, gamma ray astronomy was mainly done by satellite based instruments like FermiLAT. The Large Area Telescope, the principle scientific instrument on the Fermi Gamma-Ray Space Telescope Spacecraft sensitive in the energy range between 20 MeV and 100 GeV, launched in June 2008. fig (2)

1.1 Air shower induced Cherenkov Radiation

Because our atmosphere is opaque for gamma radiation, gamma ray astronomy was mainly done by satellite based instruments like FermiLAT. That said, we can still see their effects on earth through gamma-ray induced particle cascades. When a primary particle, i.e. a gamma photon or cosmic ray enters the atmosphere and collides with a nucleus of the air, it gets scattered and creates secondary electrons, positrons and photons. Those secondary particles also interact with the atmosphere creating a cascade of particles called a particle shower.

Shower schematic overview and propagation

In this air shower, the initial and each subsequent particle traveling through our atmosphere emits Cherenkov light. Cherenkov radiation is a phenomenon caused by charged particles traveling faster than the local speed of light would allow in that medium. This light is emitted in a narrow cone with an increasing angle as the particles travel downward. This Cherenkov light shows as a very short ($\sim 5\text{ns}$) flash with a peak in the UV-spectrum at around 330nm. Thus, we can image the particle cascade measured with the telescope and can reconstruct their path through a stereoscopic image of the shower taken by multiple telescopes(appendix 50), reconstructing the position of the source in the sky.

It is also possible to reconstruct the energy of the original photon from the amount of light produced. This is possible because energy is conserved, so all energy of the original photon is

now distributed between the particles of the shower.

To determine whether it is a hadronic shower originating from cosmic rays or a gamma shower, originating from gamma ray photons, we look at many different shower characteristics like diffusion , compactness, and the ratio of width and length.

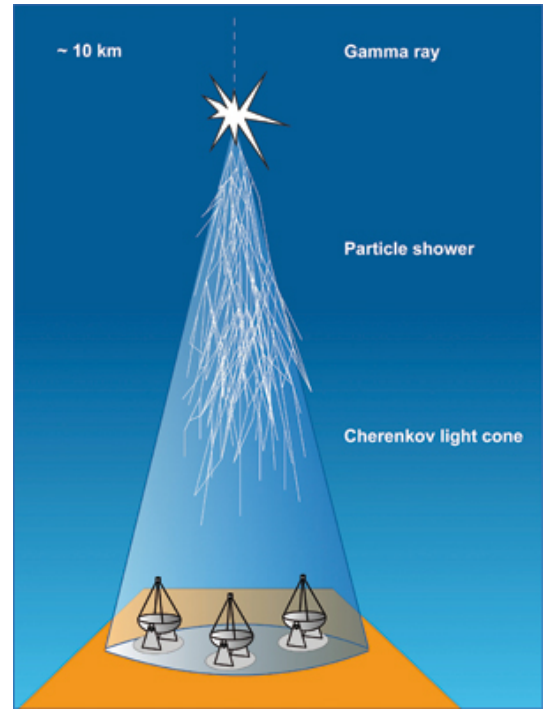


Figure 3: The cone of Cherenkov light emitted by an extensive air shower

2 Imaging Atmospheric Cherenkov Telescopes

Before, gamma ray astronomy was mainly done using satellite based instruments. The technique, pioneered by the Wipple Collaboration (US), behind the ground based experiments called Imaging Atmospheric Cherenkov Telescopes (IACTs) aims at measuring the time, direction and energy of flashes of Cherenkov light from extensive air showers caused by very-high-energy (VHE) gamma radiation. Those ground based instruments have a much larger effective detection area than any satellite based instrument, which have a typical detection size of 1m^2 . The range of the Cherenkov flash being between 300-600nm, current generation Silicon Photomultipliers (SiPMs) are a promising candidate to replace the progenitor photon detector used in previous experiments like HESS, the Photomultiplier Tube (PMT).

Current ground based IACTs consisted of mostly 4 telescopes, HESS, MAGIC, Veritas among them. (appendix51)

All of those arrays consist of at most 5 telescopes spread over a wide area. So most cascades are viewed by only 2 or 3 of the telescopes. Additionally, due to the low flux of VHE gamma radiation, detectors for this energy range are spread over a large area, making space based instruments, which detect the incident gamma ray, an inconvenient choice. Another detection concept for VHE gamma radiation are ground based air shower particle detectors such as the High-Altitude-Water-Cherenkov observatory (HAWC) [??]. They employ a similar detection principle, recording shower particles reaching arrays of ground based particle detectors filled with water as detection medium, in contrast to air in IACTs. Those have the advantage of a larger duty cycle than IACTs, as they are able to operate during the day. Their limited sensitivity even with high observation time however will not allow them to compete with the sensitivity and resolution of IACTs such as CTA. They will however be able to provide useful complementary information.

2.1 Cherenkov Telescope Array

The Cherenkov Telescope Array, CTA, is an advanced ground-based observatory array of many tens of telescopes distributed over a larger energy range than before. It will allow detection of gamma rays over a large area on the ground and from multiple different directions. The array will consist of 60 - 100 telescopes of different designs and sizes to cover the aimed for energy range and area. Science goals are the understanding of cosmic rays and their role in the universe, including the study of cosmic particle accelerators, such as pulsars, pulsar wind nebulae , supernova remnants and gamma ray binaries. Secondly particle acceleration around black holes of supermassive or stellar size and lastly physics beyond the Standard Model. There are currently 2 sites planned, which when deployed, will achieve full-sky coverage.

1. A southern cta site, with an array consisting of three types of telescopes:

- a) The low energy instruments¹, between 20 and 200 GeV, will consist of four 23 meter class telescopes with a moderate field of view (FoV) of the order of about 4.5 degrees.
- b) The medium energy range², from around 100 GeV to 10 TeV, will be covered by 24 telescopes of the 12 meter class with a FoV of 7 degrees.
- c) The high energy instruments³, operating between a few TeV to 300 TeV, will consist of about 72 small (4 meter diameter) telescopes with a FoV ranging from 9.1 to 9.6 degrees.
- d) (area covered by the array of telescopes: 4 km²)

2. CTA Northern Site:

- a) 4 large-size telescopes and 15 medium-size telescopes
- b) (area covered by the array of telescopes: 0.4 km²)

There are currently 3 different prototypes in development for the SST variant: SST2M GCT and Astri , and a single mirror prototype SST1M

This papers work is conducted on the GCT design, one of the prototypes for the high energy telescope called SST-2M GCT utilizing a 2 mirror design called Schwarzschild-Couder.

2.2 GCT

The 2 mirror design of the telescope allows us to utilize SiPMs. Current IACTs have a parabolic optical system, which is reliable and efficient but they need to be large in order to have a large FoV due to aberrations, resulting in huge CAMERA plate scales and therefore expensive assembly of photodetectors.

Schwarzschild-Couder have no such aberrations, at least not on our scale, while the IACTs can still have a very large f.o.v. up to 15° without significant degradation of the spot size. The resulting physical pixel size is more compact than that of the single mirror optics and cost-effective photon sensors such as multi-anode photomultipliertubes (MAPMTs) (like in CHEC-M) or Silicon Photomultipliers (SiPMs) can be used for the camera.

There are of course disadvantages, the optical system will be more complex, with tighter tolerances.

In summary it reduces the camera plate scale, allowing us to use SiPM photosensors.

¹ LST large scale telescope

² MST medium size telescope

³ SST small scale telescope

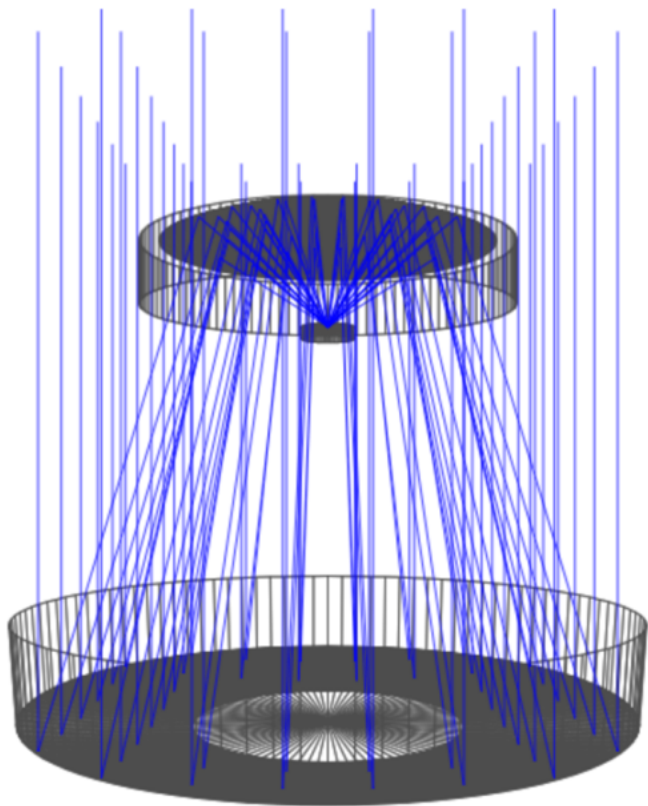


Figure 4: Schwarzschild-Couder Optics, If possible replace picture with GCT with mounted CHEC camera picture here

2.3 CHEC-S

The Compact High Energy Camera, or CHEC is one of three prototype camera concepts in development for one of the SST structures within CTA. One camera features 2048 SiPMs, building equally many readout channels per camera. The readout is done by so called TARGET⁴ modules for sampling, digitization and triggering, one of those consists of 4 ASICs⁵ with 16 channels each. The camera houses 32 TARGET modules, one of them responsible for readout of 64 SiPMs. The TARGET modules build the front-end of the integrated electronics inside the CHEC-S camera connecting the SiPM buffer to the cameras backplane. After the SiPM is triggered the buffer amplifies the signal, that is then send to the ASIC inside the TARGET module, where an analog-to-digital converter and a shaper convert the signal before it is send to the backplane for transfer to the main array hub.

2.4 SiPM requirements for CTA

In order to make an educated choice on the best SiPM device to use to populate the cameras focal plane, an in-depth characteristic study on pulse-shape, gain, temperature-dependence,

⁴ TeV Array Readout with $\frac{GS}{s}$ sampling and Event Trigger

⁵ Application Specific Integrated Circuit

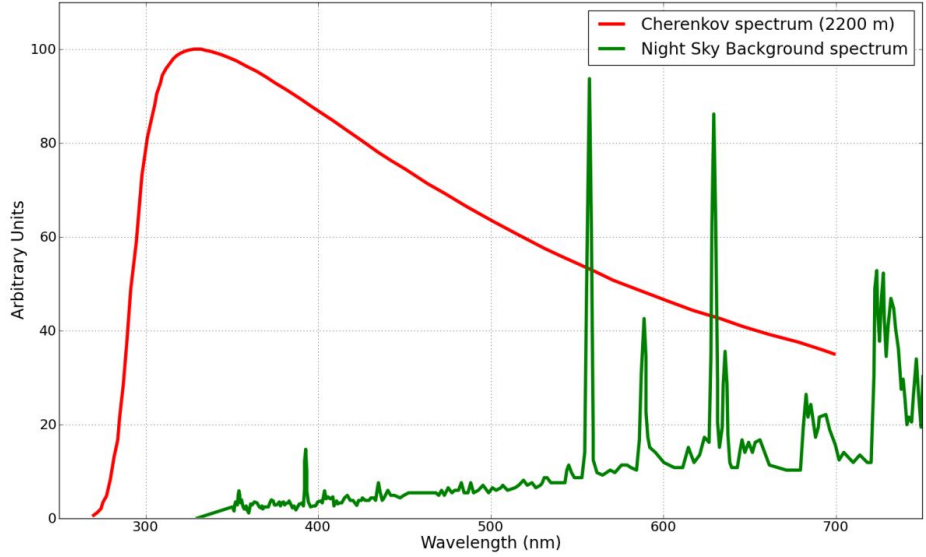


Figure 5: The spectrum of Cherenkov light observed from an extended air shower at 2200m asl. compared to the expected NSB measured in La Palma. Units on the y-axis are arbitrary because NSB and Cherenkov light vary by different parameters. Image from [11]

detection efficiency, thermal noise and correlated secondary effects is conducted by multiple groups within the CTA collaboration.

This paper studies noise from thermal, as well as correlated secondary effects and their temperature dependence. To be considered a promising candidate, any given SiPM device must have a high enough fill-factor (detector space versus dead space) to guarantee high Photon Detection Efficiency (PDE). This is necessary to ensure the data loss in CTA requirements? . The peak of the spectral response of the SiPM is desired to be around the spectral peak of the Cherenkov light and at the same time, must have a fast enough drop to ensure less Night Sky Background (NSB) pick up (Figure(??)). The overall noise from thermal and correlated secondary effects of the SiPM must be sufficiently below the expected NSB rate at the location (usually around \sim 20-80 MHz). Additional?

3 Silicon Photomultipliers



Figure 6

Silicon Photomultipliers (SiPMs) are semiconductor photo detectors, that have attracted increased attention over the last decade for their possible use in astroparticle physics. The sensor consists of an array of avalanche photo-diodes, typically $50\mu\text{m}$ in size. Depending on the pixel-size, one pixel contains several 1000 diodes, hereafter called cells. Each cell is a PN junction fig(7) supplied with a reverse bias-voltage above breakdown, which is called operation in Geiger-mode, in analogy to the Geiger counter. In this mode, a photon or thermal excitation will produce an electron-hole pair in the depleted region. Through impact ionization these charge carriers will in turn trigger an avalanche in a cell, which in turn generates a large output pulse typically in the range of several Mega electronvolt. This avalanche is then passively quenched by a resistor to limit the current in the substrate and to reset the cell to a quiet state so it is photosensitive again. The signal of the SiPM is the sum of the signal of all cells, read out over their quenching resistor via a common output.

Silicon Photomultipliers posses major advantages over their progenitor, the Photomultiplier-tubes, or PMT fig(??). They are more resistant to mechanical and accidental light-exposure damage through ambient light. Silicon Photomultipliers have a lower power consumption and, operating at a much lower bias-voltage, there is no need for high-voltage as in PMT. They posses a high photon detection efficiency and are insensitive to magnetic field changes. There is rapid improvement, being a fairly new technology, with new generations every ~ 5 months and decreasing costs per mm^2 . Viewed over all cells of the whole pixel, fluctuations in the gain are very small. This is because of the uniformity during manufacture and visible in the width and the clear resolution of the p.e. peaks in the pulse area spectrum. Examples in the appendix E. Multi anode photomultipliertubes do not posses those small gain fluctuations, which is due to their

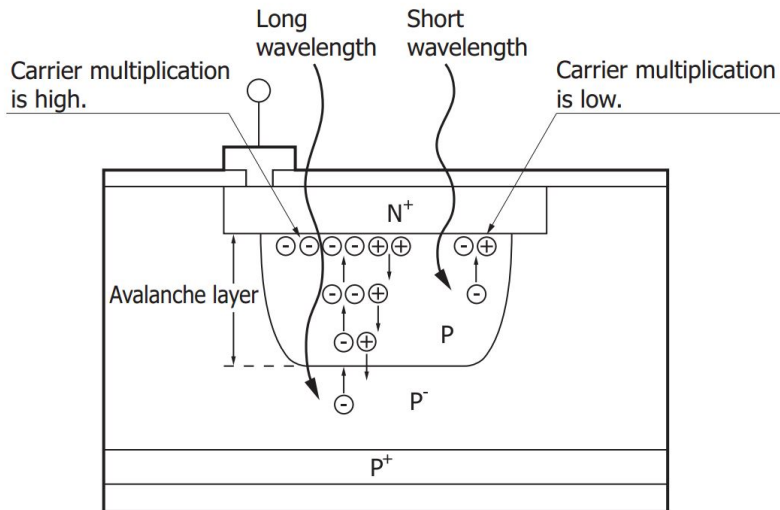


Figure 7

structure. These make Silicon Photomultipliers an interesting candidate in astrophysics experiments for both, space- and ground-based telescopes (or IACTs, Imaging Atmospheric Cherenkov Telescopes).

1. Sturdiness
2. May be exposed to ambient light (observation during bright moonlight periods possible)
3. Low power consumption ($\leq 50\mu\text{W}/\text{mm}^2$)
4. Low operation voltage (typically $\sim 20 - 100$ Volts)
5. No need for HV, as in PMTs
6. High Photon detection efficiency
7. Insensitivity to magnetic fields
8. Being a fairly new technology it is steadily improved, meaning a new generation of SiPMs every 5months
9. Rapidly decreasing cost per mm^2

The currently most challenging astrophysics experiment Silicon Photomultipliers are considered for is use in Cherenkov telescopes, with very demanding expectations in terms of photon detection efficiency. The photon detection efficiency quantifies the absolute efficiency of any photon detector to absorb a photon and produce a measurable signal at its output. To achieve a high photon detection efficiency in the 450nm regime, the design moves to very thin implantation layers on the surface in order to minimize the absorption of shorter wavelength photons in insensitive areas. Figure(??) Different entry window coatings and avalanche structures (trenches etc.) explore the capable enhancements in the blue sensitive UV region.

3.1 Gain of a Silicon Photomultiplier

The gain of a Silicon Photomultiplier measures the internal conversion of a photon incident into a signal at the output. The amplification of the device is expressed as the average number of charge carriers produced. There is no distinction whether the incident was caused by a single original photon or a thermal electron.

$$M = \frac{Q}{e} \quad (1)$$
$$Q = C * (V_{bias} - V_{breakdown})$$

Figure 8: The gain (M) of a Silicon Photomultiplier results from the deposited charge (Q) of the pulse generated from one cell when it detects one photon, divided by the charge per electron (e). The charge deposited per event is proportional to the cell's capacitance (C) and the supplied over-voltage ($V_{bias} - V_{breakdown}$). This results in the gain (M) in units of total number of charge carriers, usually in the several 10^6 range.

Estimation can be done via the voltage mean of the 1 p.e. amplitude: (e.g. see Figure (25)). For a better understanding, stating the gain in units of mV per photoelectron or $\frac{mV}{p.e.}$ is more suitable, as it gives a direct correlation between detected photoelectron and expected voltage amplitude. Given the very narrow pulse shapes, using the average pulse amplitude and extracting FWHM as a time measure of the total charge flowing during discharge and using the formula:

$$Q(p.e.) = C * (V_{bias} - V_{breakdown}) \quad (2)$$
$$U(p.e.) = \frac{Q(p.e.)}{t(FWHM)} * 50\text{ohm}$$

Figure 9: Resulting in the expected event charge flowing during capacitor discharge. Given the bias-voltage and C as capacitance of one cell, a conversion factor and the average amplitude per photoelectron can be extracted.

The gain is obviously higher the larger the cell capacitance or the higher the bias-voltage (eq ??) will be. But increasing the bias-voltage also increases dark counts and crosstalk. The gain is also dependent on the temperature, mainly through the quenching resistor but also from the silicon bulk itself, at a certain bias-voltage decreasing as temperature rises. The quenching resistor is affected by a lowering of the electrical conductivity with rising temperature, in accordance to the Wiedemann-Franz law, stating that the ratio of electrical and thermal conductivity remains

constant. The silicon bulk at rising temperatures underlies increased crystal lattice movement. This impinges charge transport by increasing the probability that carriers might impact on the lattice before the carrier energy has become large enough for continued ionization. In order to counteract this, the electric field must be increased by increasing the supplied bias-voltage so ionization is more likely. Doing this has drawbacks as discussed before. For application as a photon detector, keeping the gain constant is an inevitable step, otherwise the shifting gain leads to problems. To do that, either the bias-voltage need to be adjusted to match ambient temperature, leading to problems with varying dark counts and crosstalk. Or the surface temperature must be regulated to be kept constant. Although more challenging hardware would be required, the latter option has obvious advantages, keeping dark counts and crosstalk and more important the gain constant by simply regulating the surface temperature.

Taking into account equation ??, it appears that the breakdown-voltage can be estimated from the zero-crossing of a linear extrapolation of the gain at every bias-voltage per temperature. By doing this a linear breakdown-voltage dependence of the temperature can be observed. Appendix Figure(53)

I note that the gain, when parametrized over over-voltage, is essentially temperature independent, as I will show later in chapter 6: Figures (31) , (36) , (41) , (44)

3.2 Thermally induced dark counts

Still temp dependent when plotted vs overvoltage Inside the Silicon Photomultipliers depleted region a dark pulse originates from thermal excitation of an electron to the conduction band. Without an event photon present to trigger the avalanche, it is still indistinguishable from a photoelectron pulse. These thermally generated carriers are observed along with the signal from a real photoelectron, presenting an irreducible source of noise. The number of dark pulses observed is referred to as dark counts and the number per second as the dark count rate. For applications that need to operate in an environment with low noise, those dark counts are a concern. In IACT application of Silicon Photomultipliers however, this is only a minor problem, since IACTs operate in a naturally noisy environment. Even though sky darkness is one of the prime criteria of the proposed site selections for CTA, the surrounding Night Sky Background (NSB) at the most darkest side in Namibia will still exceed any random noise in the detector. The pollution of those NSB photons is unavoidable noise and will essentially limit the low energy resolution of the telescope to the NSB rate. As long as any random noise, being dark counts or other, is significantly below the NSB rate, it will not affect the telescopes performance.

Telescope performance simulations of the Schwarzschild-Couder MST of CTA at the site of Namibia showed a rate of $\sim 20 - 80$ MHz per pixel for one of the older SiPM iterations from Hamamatsu. [11] This is purely for NSB photons and pixels with a size of $6 \times 6 \text{ mm}^2$, the covered range originates from differences in illumination level of the night sky by galactic-

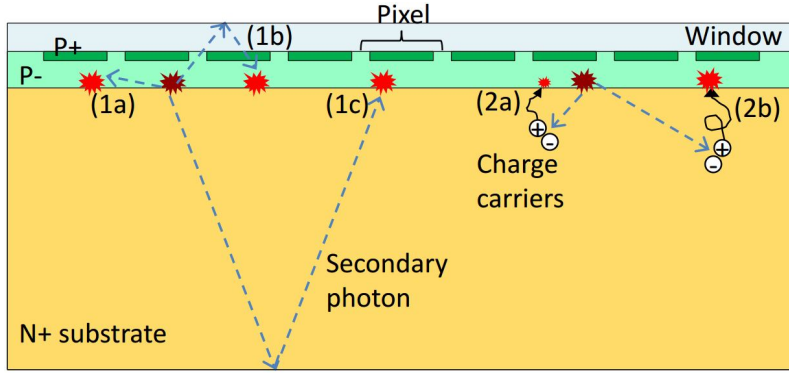


Figure 10: Secondary effects (bright red) caused by primary avalanches (dark red) in a Silicon Photomultiplier. In this paper a single pixel, in this figure, is referred to as a cell (see 3). Everything label under 1 is associated with prompt cross-talk, afterpulsing labeled as 2a, and delayed cross-talk labeled as 2b. Image adapted from [ref]

and extragalactic-fields. I note that the DCR, when parametrized over over-voltage, remains temperature dependent, as I will show later in chapter 6: Figures (32) , (37) , (42) , (45)

3.3 Avalanche-induced secondary effects

An avalanche originating from the primary cell can sometimes, either directly or by reflection, propagate outside the cell and trigger an avalanche almost simultaneously in a secondary cell. This will, unless accounted for, degrade the Silicon Photomultipliers photon counting resolution, since the signal will be a merge of cross-talk cells and real incident cells. The probability for this is referred to as the cross-talk probability and the effect as the Optical Cross Talk, since it is conveyed via secondary photons generated in the primary avalanche. Afterpulsing also falls under this category, with the main difference to cross-talk being that the carrier triggers a secondary avalanche in the primary cell, basically generating a parasitic pulse inside the previously fired cell. Contained in a single cell, afterpulsing increases the measured charge registered for an incident photon. The difference in arrival time of the secondary avalanche distinguishes different components comprising the cross-talk and afterpulsing. Those secondary avalanches can again emit photons, that can trigger secondary avalanches themselves, leading to high amplitudes, even in dark conditions.

Figure (10) shows different physical processes causing secondary effects in Silicon Photomultipliers based on their delay time. Cause of the delay time is the dependence on the penetration depth of the incident photon, or the region the dark count generated, and the diffusion time inside the substrate. At long delay times afterpulsing and cross-talk are not distinguishable. The prompt Optical Cross Talk happens basically simultaneous to the primary avalanche, since it is unaffected by the primary cells recovery time and is labeled 1 in Figure (10). It is either triggered by the secondary photon directly (1a) reaching the neighboring cell, or after first re-

flecting on the surface layer (1b) or the bottom surface (1c). If the cross-talk avalanche delay time is shorter than the detection resolution, the difference in signal between an Optical Cross Talk event or an incident photon being detected, is not observable.

Time delayed Optical Cross Talk is caused by a carrier generated in the non-depleted substrate diffusing to a neighboring cell and triggering an avalanche in the depleted region (2b). If the carrier stays in the primary cell, the triggered avalanche is labeled afterpulsing (2a) and will have a lower amplitude, due to the cell not being recovered yet. The delay time is influenced by how deep the carriers are being trapped in the substrate, the time they need to diffuse to the surface, and also distinguished by traps with different lifetimes.

This is very important in IACT performance, since this effect gives random NSB and dark count photons the ability to rise to arbitrarily large amplitudes. The consequent need to raise the trigger threshold to counteract the resulting rising accidental-trigger has a negative impact on the low energy resolution of the telescope.

Parametrized with over-voltage, the secondary avalanche effects are temperature independent, shown in chapter 6: Figures (33), (38), (42), (45)

3.4 OCT dependency on cellsize

Cross-talk is dependent on the ability of the secondary photons to reach a neighboring cell. This means, that an increase in cell-size and therefore cell-area should directly correlate with the Optical Cross Talk of a pixel. In Figure (11) the results of the complete Optical Cross Talk of 2 sets of $50\mu\text{m}$ and $25\mu\text{m}$ HPK S13360 devices are shown. Plotting the results of 2 similar devices, only different in their cell-size, and then multiplying the $25\mu\text{m}$ results by the factor derived from their difference in area, here 4, a correlation is visible. Scaling up the Optical Cross Talk of the $25\mu\text{m}$ cell, shows an overlap between the 2 cell-sized pixels. This means, that the Optical Cross Talk is directly area and therefore cell-size dependent. Research by J. Rosado and S. Hidalgo [12] on the cross-talk probability of Hamamatsu SiPMs showed through Monte Carlo simulation, that the prompt crosstalk mostly takes place in a small area of pixels (~ 8) around the primary one. Which means, that the cross-talk is directly increasing with increasing cell-size, or in other words: with chance to diffuse to a neighboring cell. Small cells reduce the chance, as there is less area to a neighboring cell to pass through.

Since the measurements conducted by me do not differ between the range of secondary avalanche effects, the Optical Cross Talk shown contains every aspect, prompt and delayed as well as afterpulsing.

3.5 Photon Detection Efficiency

The Photon Detection Efficiency is the probability of a detector to absorb an incoming photon and produce a measurable signal at its output, and depends on a number of factors. First the

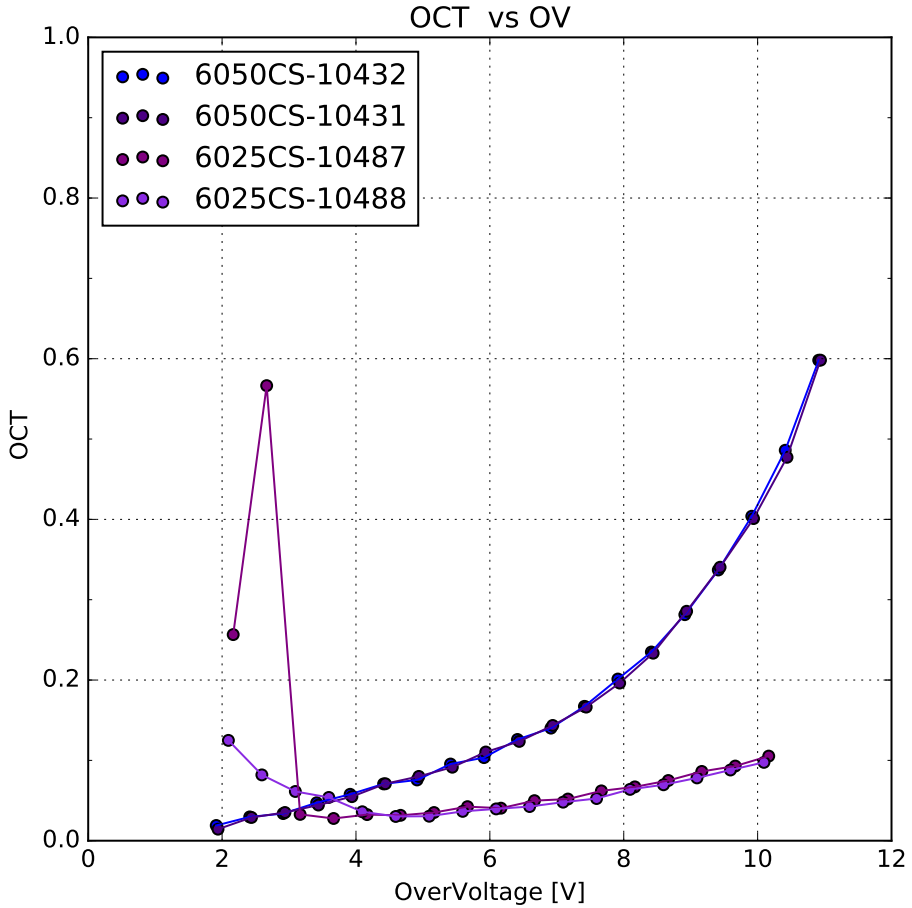


Figure 11: Results of the Optical Cross Talk of 2 sets of 2 similar HPK S13360 devices, that only differ in their respective cell-size. HPK S13360 is the first device incorporating physical trenches in the upper layer, optically isolating each cell. Consequence to this is a drastic reduction in prompt cross-talk. Delayed cross-talk and afterpulsing are basically unaffected. Upscaling the 25 μ m results shows an overlap between the 2, see text.

photon must enter the depleted region via transmission through the surface of bare silicon, which has a reflectivity of 30%. However, the transmission probability can be improved by coating the surface with a substrate with adequate thickness and a refraction index between air $\eta_{air} = 1$. and silicon $\eta_{silicon} = 3.4$. Devices presented in this paper are coated with epoxy, a silicon resin and glass. The coating also has the added benefit of insulating and protecting the cells against environmental influence. A possible negative effect of coating is an increase in prompt cross-talk and a larger dependency of the overall cross-talk on the cellsize. The second factor is quantum efficiency, describing how susceptible the depleted region is to photons exciting electrons from the valence band to the conduction band. This is sometimes referred to as spectral response of a detector to reflect the wavelength dependence of a detector and makes the PDE wavelength dependent. The over-voltage dependency of the PDE is conveyed by the third factor, the avalanche probability. It depends on the electric field present, and thus on the

applied over-voltage. The last factor is the fill-factor: the more the surface area of the detector is covered with active-area cells and the less dead-area exists between cells the higher the fill-factor is.

The Photon Detection Efficiency is commonly measured by illumination of the pixel and a calibrated reference photodiode with a flashing light source, and determining the average number of photons hitting the photosensor during a light pulse.

$$PDE = \frac{N_{detected\ photons}}{N_{total\ photons}} \quad (3)$$

Figure 12: Photon Detection Efficiency is the percentage of detected photons versus overall emitted photons.

4 Experimental Setup

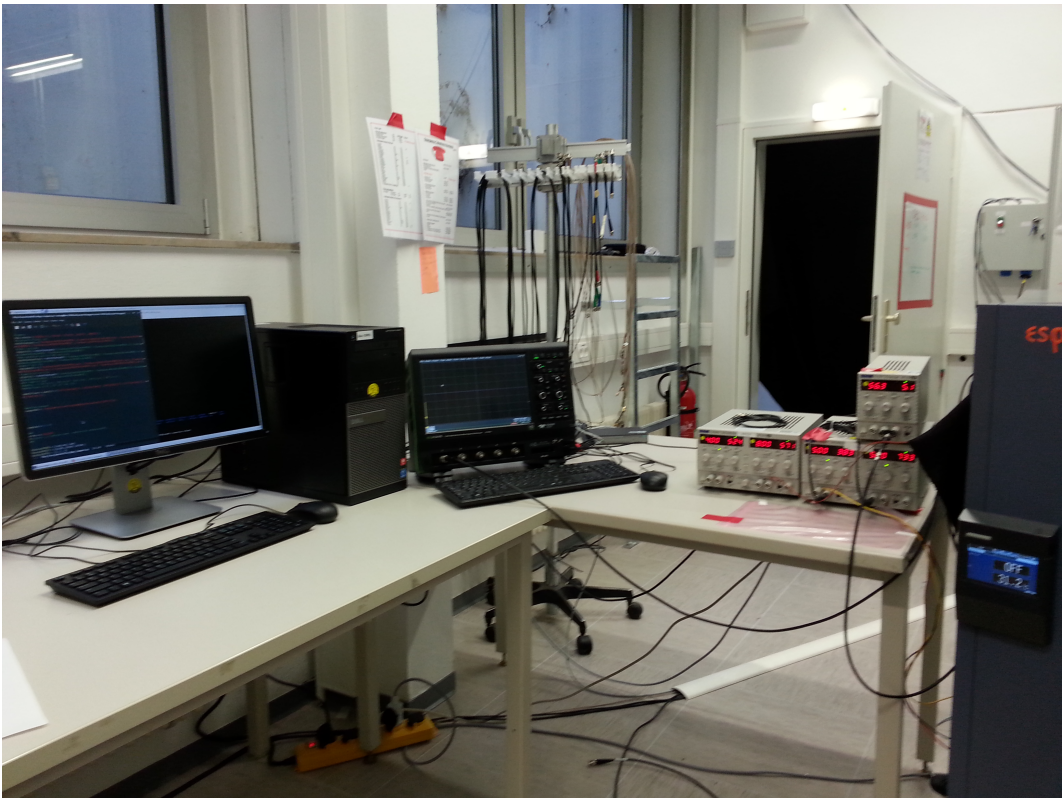


Figure 13: Will be updated. With Alphabetical captions for the different steps and references later in the text and setup scheme below, Picture of the inside of the thermal chamber is missing, will do later, and try to fit it next to this one

The experimental setup in general is designed to house a variety of SiPM devices. Over the course of this paper, 5 different types of SiPMs were mounted on the setup and evaluated. It involves a thermal chamber Figure(14)(A) for temperature regulation which proved light tight and thus also serves as a dark box, to prevent any stray light to reach the SiPMs surface. Depending if the SiPM Figure(14)(A1) in testing is pre-manufactured on a test-array or supplied as a standalone chip, it is either mounted directly on a mechanical arm inside the chamber in the former case, or in the latter the mechanical arm supports a specifically designed PCB connecting to the device. Via the mount, bias-voltage is supplied and signal is transferred to the shaper Figure(14)(A2). !!!!!Need some more details on shaper

In some cases the output signals amplitude is too low to trigger the oscilloscope, therefore amplification is needed. I used an amplifier from MiniCircuits ZFL-1000-LN+ SN:283401542 Figure(14)(A3) supplied with different voltages depending on the tested device to amplify the shaped signal.

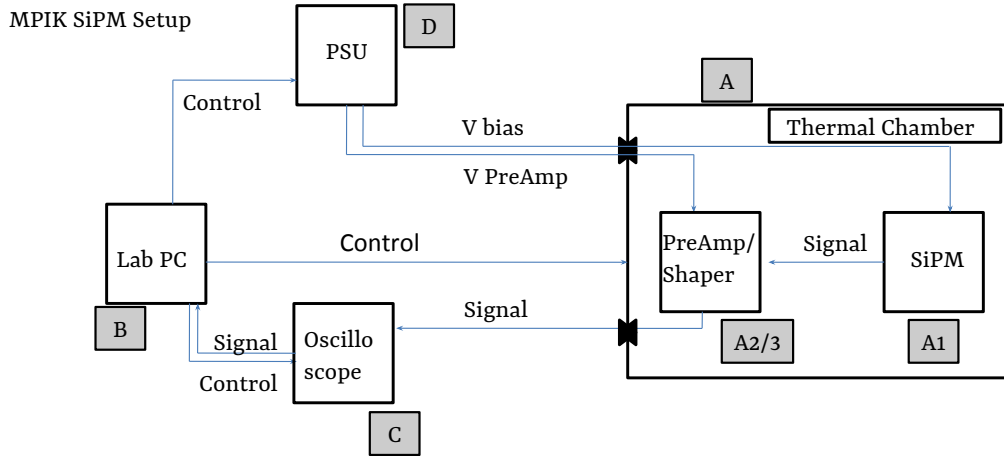


Figure 14: Experimental setup scheme

Data acquisition in the Laboratory is realized by a Lab-PC Figure(14)(B) , that forms the central control station for multiple pieces of equipment. It is connected to the oscilloscope Figure(14)(C), which records the waveforms of the device in testing, and then sends the data back to the PC via ethernet. The oscilloscope is a Lecroy XXXXX SN capable of $2.5 \frac{GS}{s}$. The power supplies Figure(14)(D) control the bias-voltage of the Silicon Photomultipliers, ramping of the bias-voltage is controled by the PC. Lastly the thermal chamber is connected to the Lab-PC, which controls the temperature, and continuously rechecks it during temperature ramps. Signal transfer from the shaper to the oscilloscope is via a throughput on the side. All equipment is connected via ethernet, plugged into a common hub, to form a local network. While the temperature of the thermal chamber is ramping from the previous to the next set-point, the data is send to the Lab-PC.

Temperature regulation is an issue in the teststand, as there is no way of controlling the SiPMs surface temperature. In dark conditions however, without conducting illumination tests, the shift in temperature on the SiPMs surface is only minimal. (Find the breakdown-voltage dependence on temperature in the appendix (??)). Checking the surface temperature of all devices with a temperature probe during testing showed minimal rising temperatures. So the influence of the temperature on the breakdown-voltage is only of minor concern. However, once illumination tests begin, the rising temperature on the SiPMs surface will no longer be negligible and the temperature must be regulated, either by cooling of the surface or including the temparature parameter.

5 Data Analysis

The analysis of the Silicon Photomultiplier waveforms is done exclusively in python following the sequence:

1. data conversion
2. pedestal subtraction
3. peak detection
4. gain extraction
5. calculation

The waveform data, after being transferred to a separate PC, is analyzed offline. The goal is to extract event-data from the waveforms in order to produce pulse-area spectra for every bias-voltage at every temperature. To that end, the pedestal of the electronic noise must be found and subtracted from the data. After that, event-pulses are detected and integrated. This generates a list of pulse-areas, which is in turn used to fill a pulse-area histogram. To this pulse-area histogram, a model is fitted from which the gain can be extracted. Due to the linear behavior of the gain with rising bias-voltage, a regression line is fitted, from which the Dark Count Rate and the Optical Cross Talk are calculated using the original pulse-area histogram.

5.1 Tracefile Conversion

The oscilloscope produces the waveform data in its intrinsic data format, called a trace with the data suffix trc in binary. A trace file contains a header and two binary lists, an amplitude based on the oscilloscope's voltage-range and offset, and a list of the same length containing the associated event-time, based on the time-range and horizontal offset. The first step is therefore a conversion of the amplitude and associated event-time of all segments of a waveform trace file into two lists of floats.

5.2 Pedestal Subtraction

A single waveform from the oscilloscope is anticipated to be uncentered fig(15)(grey), it will be slightly above or below zero, depending on the device setup (some devices produce inverted signals). The signal is mixed with electronic noise when it is observed and forms a pedestal, shifting the mean of the waveform from its original position to zero. Pedestal subtraction removes this average noise.

The first step of the process is reading in the uncentered waveform fig(15)(grey) and calculating an initial mean(mean0), expected to be slightly higher than the actual mean of the noise, due to the presence of event-pulses. The waveform is then shifted to about zero, by subtracting the mean0. A second mean of the now nearly centered waveform is taken (mean1). Now a new, same-sized array is formed and filled with the data from the waveform that is smaller than mean1, this represents the negative part of the noise. The data larger than mean1, the positive noise, is also filled into the array, but is negative-signed. This creates an array of the waveform centered around zero and, above the mean1, folded towards the negative. It proved reliably, that calculating the root-mean-square of this helper-array is a solid possibility of stripping the waveform of event-peaks. Taking the root-mean-square with a factor 3 of the helper-array, a cut is now applied to the waveform on both, the positive and negative side. In that fashion, the remnant is the waveform between the positive and the negative root-mean-square and is now called a peakless-signal, representing the noise of the waveform.

Pedestal subtraction is done by calculating the mean of this peakless signal and subtracting it from the waveform. After that, the peakless signal is also smoothed by convolving it with a wide-windowed gaussian and subtracted from the waveform to eliminate any slow moving noise, the resulting waveform is called "Filtered Signal 1" fig(15)(blue).

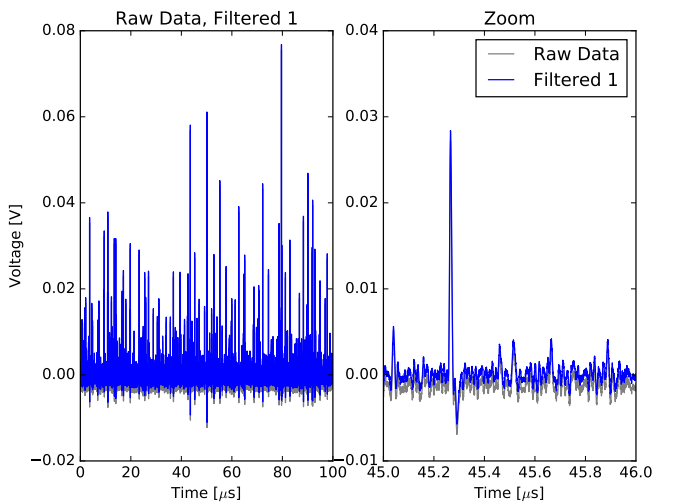


Figure 15: Pedestal subtraction++

5.3 Peak Detection

Peak detection exploits the fact, that the first derivative of an event-peak will cross zero into the negative at the time of the peak maximum. The presence of random noise in the signal however will lead to many false detections. Therefore, before the detection of the event-peaks, the waveform fig(16)(grey) is smoothed with a narrow-window gaussian with a width of about the FWHM of the devices characteristic event-pulse, in order to attenuate non-event peaks fig(16)(blue). After the first derivative of the signal is calculated, which in python is a fast process if using arrays, a number of parameters decide the validity of the detected peaks. Most important parameters are a certain predetermined minimum amplitude, called the amplitude threshold or: minimum peak height. This is right now determined by eye, but could later be calculated based on the noise level. The second important parameter defining validity is the minimum peak distance, which defines how close two events can occur after another. The value is determined by the FWHM of the device in testing, which I expect to be sensible enough to resolve two events happening close after another. The peak detection algorithm can not distinguish between instantaneous and delayed Optical Cross Talk, but nonetheless, due to the fact, that the signal data is taken over many micro-seconds, all events are detected, independent of their source. On the other hand, this also means, that it is possible for two events to happen at the same time, for example a real photoelectron-event coinciding with delayed Optical Cross Talk. This can not be distinguished and will lead to a slight shift of the amplitude. (because delOCT is partial 1p.e.)

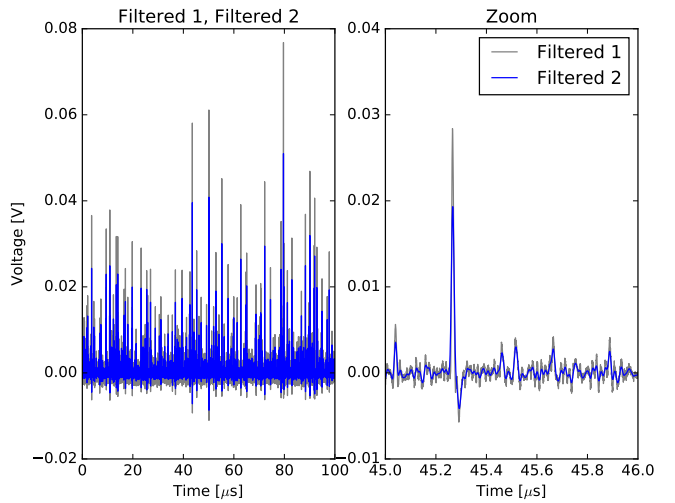


Figure 16: Peak Detection

5.4 Gain Extraction

The detected peaks are integrated with a window extending symmetrically from the peak maximum, the width is chosen as slightly wider than the peaks FWHM. The generated list of peak areas is generating a peak area histogram, which is fitted with multiple gaussians using iMinuit in python , seen in Figure (??). Two parameters are extracted from the fit to the peak area histogram. The first, the position of the 1p.e. peak is the position of the maximum of the first peak in the histogram, and the position of corresponding multiple p.e. events should be integral factors of the 1p.e. position. This proved to not be the case for some devices, the suspected source of this error is a pedestal generated during the peak integration. I studied the effect of the integration window in more detail in chapter 5.5.1. A second parameter is extracted from the peak area histogram to deal with this problem, which is the distance between N p.e. peak maxima of the histogram, labeled $\Delta p.e.$, which defines the gain. The apparent pedestal of the pulse area histogram makes extraction of the two parameters necessary in order to calculate the Dark Count Rate and the Optical Cross Talk.

The gain of a Silicon Photomultiplier has a linear dependence of the supplied bias-voltage. Given that the bias-voltage range is deliberately chosen such that the overvoltage ranges from about 1V growing upwards, the range of linearity only starts at around the point of operation given by the manufacturer of the device. At the higher end of the bias-voltage range the behaviour usually starts to divert from the linearity. In order to get an estimation of the gain over a large range, both previously extracted parameters, the 1p.e. peak and the distance $\Delta p.e.$ are fitted with a linear regression line. The fit assumes linearity utilizing weighted least

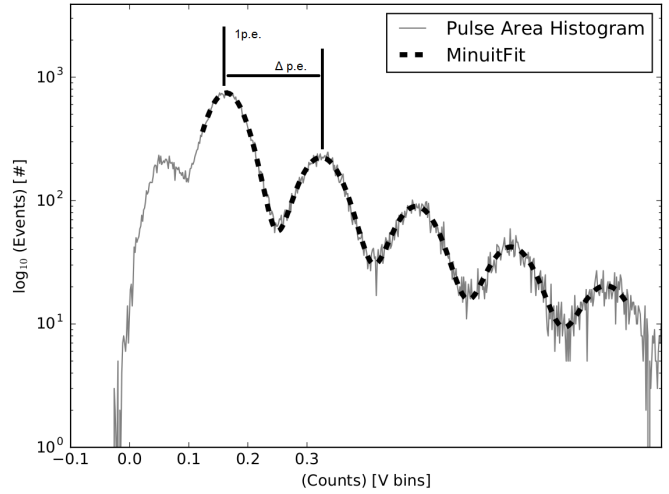


Figure 17: Pulse Area Histogram todo describe more

Pulse Area vs Vb

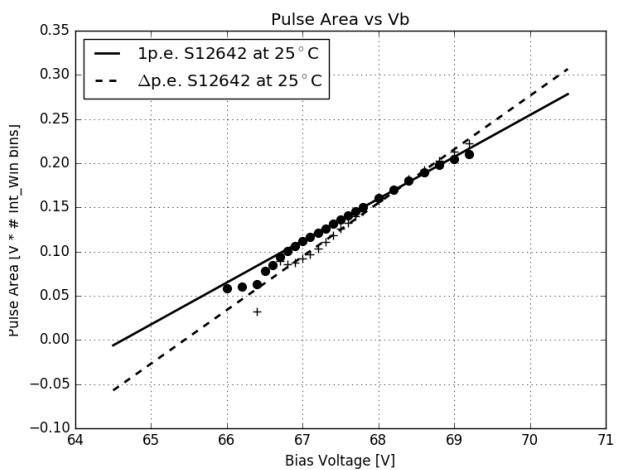


Figure 18: 1p.e. position and $\Delta p.e.$ plotted versus bias-voltage

squares inherited from pythons statsmodels package. For the fit, only the data, where at least 3 gaussians are fitted to the peak area histogram is taken into account. Plotting both extracted parameters, as well as their respective regression lines versus bias-voltage, as in Figure (18), shows the difference between the two parameters. (SHOW FOR ALL DEVICES IN APPENDIX???). Comparing the manufacturer supplied breakdown-voltage from the datasheet for all devices showed, that the zero-crossing of the 1p.e. regression line is more consistent with datasheet values, in contrast to the zero-crossing of Δ p.e. , which lies slightly higher. The over-voltage, corresponding to the set bias-voltage at any given temperature is calculated from this breakdown-voltage. Dark Count Rate and Optical Cross Talk are calculated utilizing 1p.e. position and Δ p.e. derived from the regression line. Both values are applied, in the calculation, to the peak area histogramm with the Dark Count Rate being defined as:

$$DCR = \frac{N_{events(>0.5p.e.)}}{T_{experiment}} \quad (4)$$

Figure 19: The Dark Count Rate of a Silicon Photomultiplier is defined as all events exceeding 0.5 p.e. in amplitude $N_{events(>0.5p.e.)}$ occurring over the experiment time $T_{experiment}$. Included in the measurement are thermally generated dark counts, as well as delayed cross-talk and afterpulsing with only a minor contribution.

,and the Optical Cross Talk as:

$$OCT = \frac{N_{events(>1.5p.e.)}}{N_{events(>0.5p.e.)}}. \quad (5)$$

Figure 20: The Optical Cross Talk of a Silicon Photomultiplier is defined as all events exceeding 1.5 p.e. in amplitude [$N_{events(>1.5p.e.)}$] devived by all events exceeding 0.5 p.e. in amplitude [$N_{events(>0.5p.e.)}$]. It scales with the number of photons produced inside an avalanche, as well as the probability of these photons to trigger a neighboring cell

5.5 Data Challenges

5.5.1 The influence of the minimum peak distance

The influence of the minimum peak distance is shown in Figure (21) . Based on their bin-width, four different windows are tested. With the oscilloscopes sampling rate of $2.5 \frac{GS}{s}$, the windows of 100, 63, 25 and 13 time-bins, correspond to 40, 25, 10, 5 ns windows respectively. With a

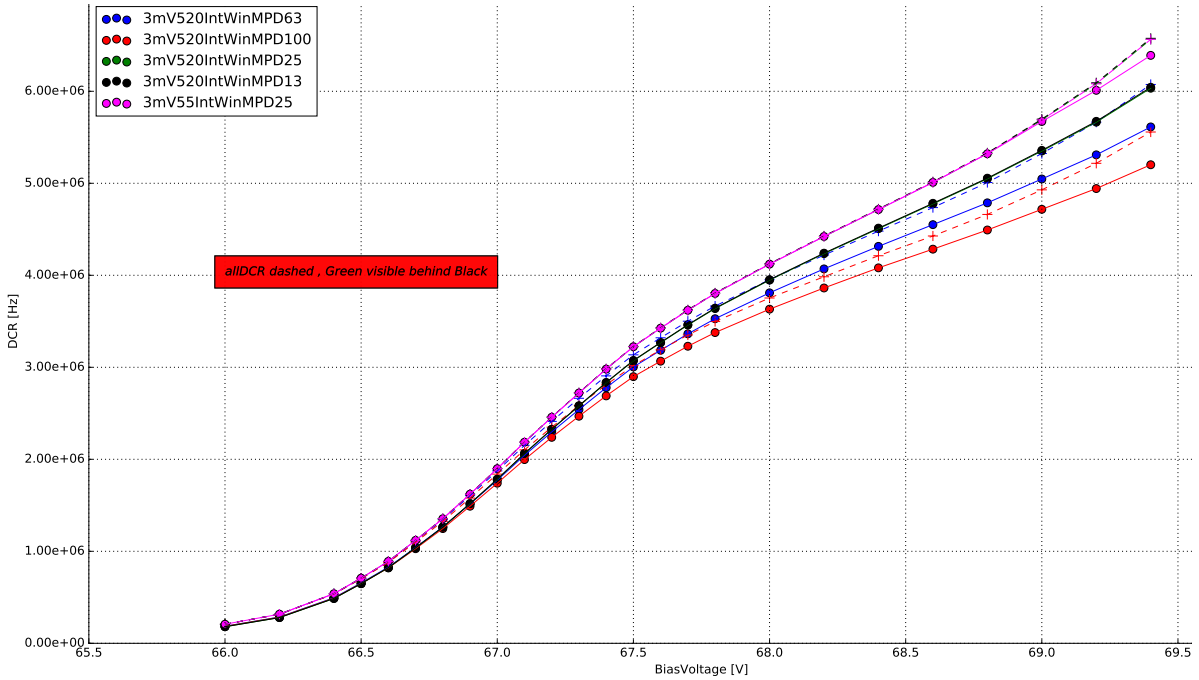


Figure 21: The difference between 4 minimum peak distance windows, in time-bins, during the peak detection. The dashed lines are the Dark Count Rates considering all recorded events, forming an upper limit. In pink, the effect of a different integration window is shown.

event pulse FWHM of 10ns, setting the minimum peak distance to 100 bins, resulting in a 40ns window is visibly to large, as the algorithm will skip over valid data Figure (21)(red). After an event is detected, skipping over 40ns worth of data will result in errors of the Dark Count Rate, since the calculation uses the complete experiment time. Therefore a more reliable distance window must be chosen. The second window of 25ns was the next approach, originating from the length of the pulse-tail Figure (21)(blue). This would lead to no detected events overlapping with the tail of one previously detected, resulting in a sharper pulse-area spectrum. Compared to a window of approximately the pulse FWHM, the previously discussed window would still lead to lost event-data. Since the sharpness of the pulse-area spectrum is already sufficient, a window around the pulse FWHM was chosen as reference for all measured devices Figure (21)(green). Going lower than the pulse FWHM showed no improvement Figure (21)(black).

5.5.2 The influence of the integration window

Figure (21) also shows the influence of the size and shape of the integration window on the Dark Count Rate. The influence of the chosen integration window is most visible in their respective pulse area spectra. Choosing a narrow, symmetrical integration window of 5ns left and right of the peak maxima, the noise peak, or zero-peak, is much more prominent compared to the pulse area spectrum of a symmetrical 10 ns window. This leads to errors in the multi-gaus fitting step, or the fitting will fail altogether. An asymmetrical integration window of 5ns left, 20ns

right, to capture the influence of the pulse-tail proved, at first, to be the best solution as their was no visible zero-peak present. The low amplitude pulses are averaged out by the extended integration window to the right of the pulse-maximum. The downside of the asymmetrical window is the shifting of the pulsle area spectrum and the fact, that the N p.e. peaks get blurred. The next step was widening the window on both sides. This proved the best solution, since there is no zero-peak visible and the N p.e. peaks are gaussian shaped. Please see the Appendix for the respective plots of pulse area spectra of the different windows C.

5.5.3 The influence of the peak detection threshold

Choosing an adequate peak-finding threshold is a crucial step. Lowering of the threshold to ~ 0.5 p.e. will cause the peak finding algorithm to misinterpret a lot of noise peaks as actual dark incidents. This, of course, leads to errors in the gain extraction and even if a gain regression line can be extracted, the resulting Dark Count Rates and Optical Cross Talk will be incorrect. Figure (22), shows the effect a low peak finding threshold has on the Dark Count Rate.

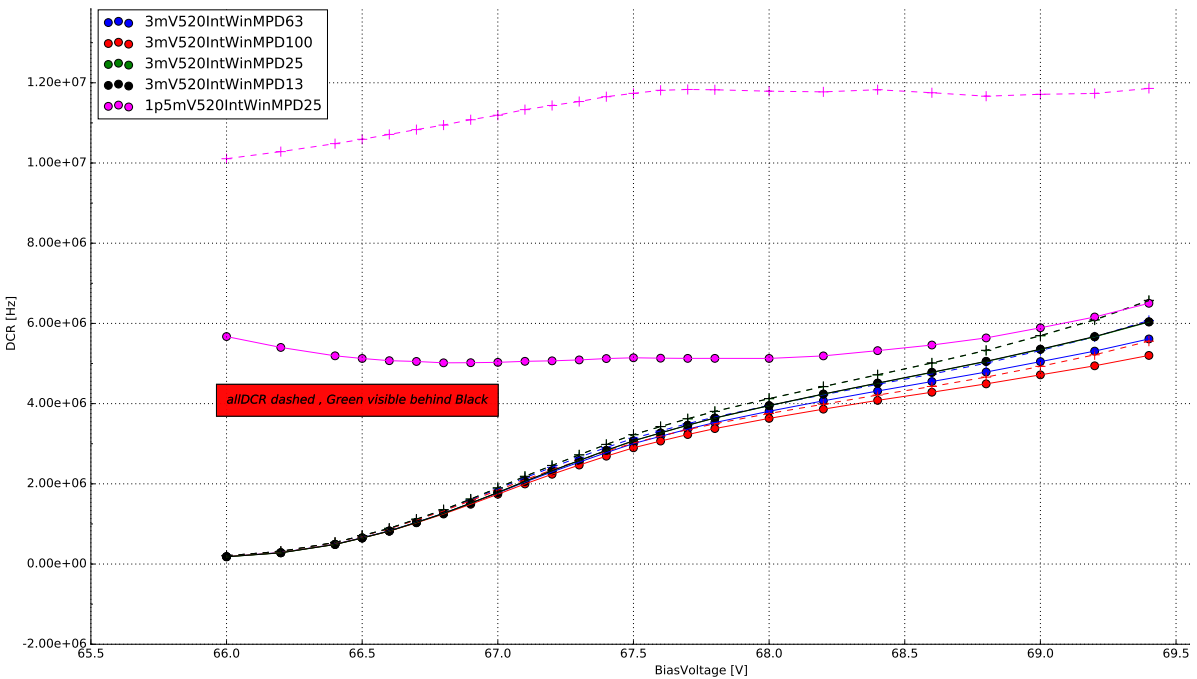


Figure 22: The difference between 4 minimum peak distance windows, in time-bins, during the peak detection. The dashed lines are the Dark Count Rates considering all recorded events, forming an upper limit. In pink, the effect of a lowered peak detection threshold is shown.

6 Results

6.1 SiPM devices for CTA

Manufacturer	pixel size	cell size	coating	connection	specifics	pre-Amp
HPK S12642-1616PA-50 *CHEC-S SiPM	3mm^2	$50\mu\text{m}$	SR	TSV	no trenches	CHEC-S buffer
HPK LCT5 S13360-6050CS	6mm^2	$50\mu\text{m}$	SR	wire-bonds	trenches	MS 13V
HPK LCT5 XXXXXXXXX	6.915mm^2	$75\mu\text{m}$	SR	wire-bonds	trenches	MS 8V
HPK 6050HWB-LVR-LCT	6mm^2	$50\mu\text{m}$	SR	TSV	trenches	MS 13V
SensL FJ60035	6mm^2	$35\mu\text{m}$	glass	TSV	no trenches	MS 15V

Figure 23: List of SiPM devices which results are presented in this paper. *(SR: silicon resin , MS: MiniCircuits , TSV: through silicon via)

Silicon Photomultiplier devices for CTA are researched by many different groups, validating different characteristics. Besides the current SiPM for CHEC-S, newly developed prototypes offer a diverse range of pixel- and cellsizes. The majority of the devices are tested in Japan, at the University of Nagoya, conducting in depth analysis of the characteristics over a wide over-voltage range at one static temperature, mainly focusing on PDE and OCT, and their correlation. This correlation of OCT and PDE for all devices determines the candidate for CHEC-S, by comparing the highest PDE at the lowest possible OCT for each device. At MPIK, chosen candidate devices are examined regarding their temperature dependence and as to assist in the final decision by confirming results with a different analysis technique.

The chosen devices include the current CHEC-S device HPK S12642-1616PA-50, from Hamamatsu Photonics K.K., to be implemented in the first prototype camera. It is a previous generation SiPM, which was decided for use in 2014.(, due to the limited availability in high PDE devices at that time.) The manufacturer supplies a 16*16 channel premounted tile of 3mm^2 pixels with a cell-size of $50\mu\text{m}$. To emulate the usage in a TARGET module, 4 3mm^2 pixels are electrically connected to form a 6mm^2 superpixel. The tile is typically coated with epoxy resin, but due to specific requirements regarding the uniformity of the coating, it was replaced with a very thin layer of silicon resin equivalent to later prototypes. The CHEC-S devices electrical connection is realised via the new through-silicon-via (TSV) concept of running a connecting solder through the silicon bulk, instead of wiring on the outside, greatly increasing the fill-factor, but also including some disadvantageous sideeffects later shown.

Additional tested devices include the LCT5 generation from Hamamatsu Photonics K.K., so called due to their low cross talk properties, namely the commercial available S13360-5050CS. This device is the first to include physical trenches between the cells, effectively dividing the cells optically and thus reducing prompt cross-talk probability.

The LCT5 generation also made two prototype devices available for testing at MPIK, the first, HPK LCT5 SN CATANIA, is a larger iteration with a cellsize of $75\mu\text{m}$ and a pixelsize of 6.915mm^2 . Being from the LCT5 generation it also includes optical trenches. The second device available is a LCT5 prototype designated 6050HWB-LVR-LCT , LVR meaning low-voltage-range, with the same physical dimensions and properties as the S13360 device but incorporating TSV technology and possibly other unknown deviations.

The final device is a commercially available test-array designated FJ60035 from SensL, pre-mounted on a test-array by the manufacturer. It has the same pixel-size, but a much smaller cell-size $35\mu\text{m}$ than the previous mentioned devices and a different coating (glass).

The tests conducted in Nagoya contain many different iterations of the LCT5 generation with varying pixel- and cell-sizes.

For a full overview of the considered Silicon Photomultipliers, please refer to the appendix under (??).

6.2 Hamamatsu S12642-1616PA-50 50 μ m 3mm

The Silicon Photomultiplier by Hamamatsu Photonics designated S12642-1616PA-50 is a 3 mm by 3 mm device. The array uses the through-silicon-via technology, meaning there are no wire-bonds present, the electrical connection is realised through the silicon-body. The pixels are coated with a thin film of silicon resin, after the previously used epoxy resin proved not uniform enough. One array consists of 256 pixels, 4 of which are electrically tied together to form a 6mm by 6mm superpixel respectively. This practice is necessary for the pre-production camera CHEC-S, because the focal plane is mechanically designed to house 64 6mm² pixels, connected to the TARGET modules. Furthermore I expect this to have an influence on my results due to electrical crosstalk, but this is only of minor concern due to the following.

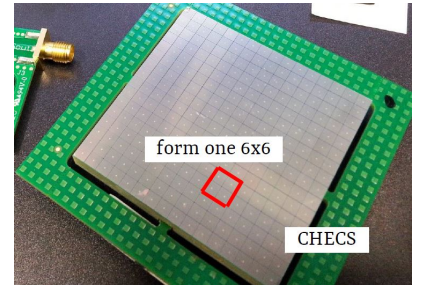


Figure 24: CHEC-S tile

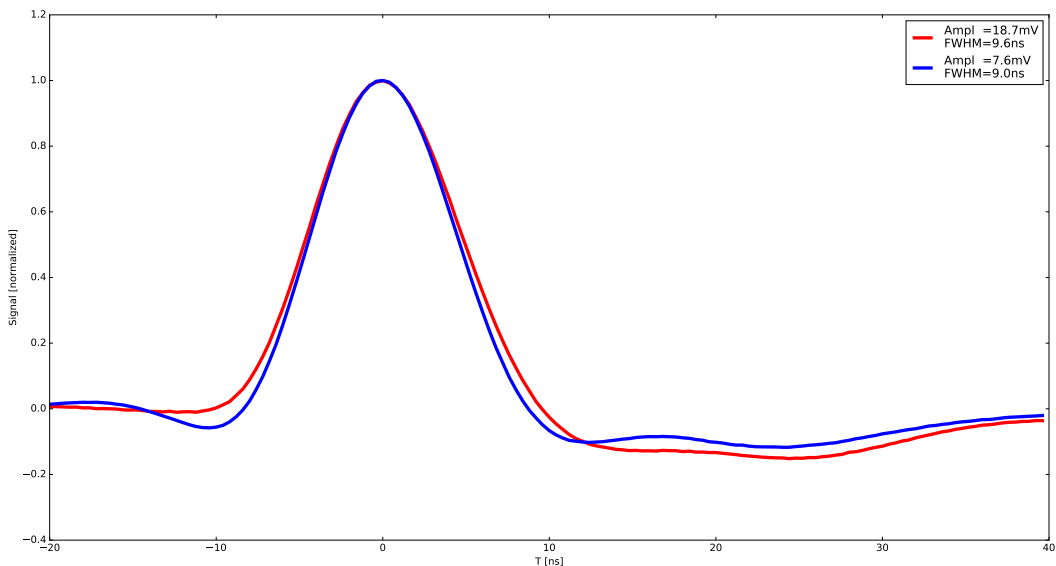


Figure 25: The average pulse shape of the 1photoelectron in blue and the 2photoelectron pulse in red of HPK S12642 at 25° C and 67.8V, which is around the proposed operating point. Both pulses are averaged over »1000 events and normalized to illustrate possible differences in pulsedshape resulting from the utilized shaping electronics. Both pulses have a FWHM of around 10ns and are nearly free of ringing. The resulting average amplitude of the 1p.e. pulse is later used to calculate the Gain in [mV/p.e.] instead of [V*IntWin] by cross-referencing the 1p.e. amplitude at multiple bias-voltages.

My measurements of the CHEC-S tile concentrate on the array as an as-is device. This means all results, influenced by external factors outside the actual Silicon Photomultipliers physics, are valid on the assumption, that the way I was conducting the measurements is the way the

Photomultiplier will later be incorporated into the camera. On that ground, deviations of my results from the results of other groups and the manufacturer itself are expected. To clarify this further, I expect, for example, that the tests done at Hamamatsu Photonics where conducted on a single 3mm^2 pixel, not an array of 256 pixels, where 4 are tied together. Also divergence of shaping and amplification electronics between the groups will result in some differences. For this test, the CHEC-S tile is connected to the CHEC-S buffer, supplied with $\pm 4\text{V}$, where the signal is amplified. This signal in turn is then shaped via the CHEC-S shaper, developed by the University of Leicester. This is done in order to lower the unshaped pulse from a FWHM in the 100s ns to 10ns. This whole amplification and shaping chain is simulating later usage in the TARGET modules. I conducted the measurements multiple times on different pixels of the CHEC-S tile (appendix555657).

6.2.1 Gain

As described in section 3.1, the average pulse shape fig(25) is used to convert the relative gain from the analysis procedure to an absolute gain in sensible units. This is necessary, because the analysis aims to use pulse-area rather than -height, which results in this relative gain being in units of $V * \text{timebins}$, instead of plain V. In Figure (??) (left) the relative gain is shown, the right side shows the gain after conversion. A lower gain with increasing temperature is expected and described in detail in the chapter 3.1. In short, increased lattice movement due to higher temperature hinders photoelectron transport. The effects visible at extreme bias-voltages at both ends are partially analysis related. The gain of a SiPM is expected to be linear over bias-voltage at a constant temperature.

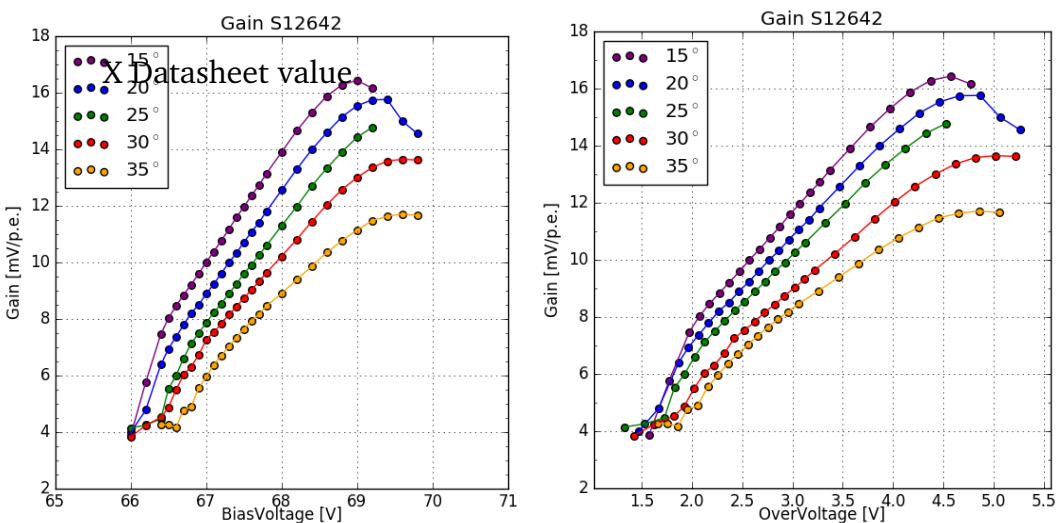


Figure 26: Gain of the HPK S12642 pixel, plotted against over-, bias-voltage and temperature.

In the lower regime at $V_b = 66.5\text{V}$ my analysis method struggles to pick up pulses, because of the very low gain compared to the noise. Depending on the chosen peak-finding threshold, I expect the analysis to interpret noise peaks as 1p.e. peaks at an increasing rate, the lower the

overvoltage is. This is visible in the sudden break in linearity at 30° C and 35° C , where the gain is almost in a plateau, due to this effect. The roll-over of the gain at the highest bias-voltages is in part a result of a voltage drop across the bias resistor occurring, because of high current flow through the SiPM. At higher temperatures, and therefore higher dark rates, the effect occurs at lower over-voltages. A second influence is caused again, by the noise at V_{ov} 5V, which is very high compared to the proposed point of operation at V_{ov} 3V. The same threshold is again counting the now increased noise peaks as 1p.e. peaks, but due to the abundance of 1p.e. pulses this just results in an apparent lowering of the gain.

6.2.2 Dark Count Rate

The Dark Count Rate is expected to increase with temperature, which is the case for S12642 shown in Figure (27). I also expect it to follow a nearly linear progression, a sudden turn-up or turn-down of the Dark Count Rate would be analysis related. The turn-up at a certain point is visible in Figure (27), particularly for 15° C (purple) and 20° C (blue) respectively. At 15° C and an Overvoltage of 4V, the Dark Count Rate starts to deviate from the previously linear behaviour. It starts to rise more rapid than before, which I can attribute to the fact, that the Optical Cross Talk at that point is very high; higher than 50% fig(28) (left). I suspect that I do not reach this critical point for the higher temperatures of 25° C (green) and 30° C (red), so the effect is barely, if not at all visible. At 35° C (yellow) I suspect my analysis is not able to count every

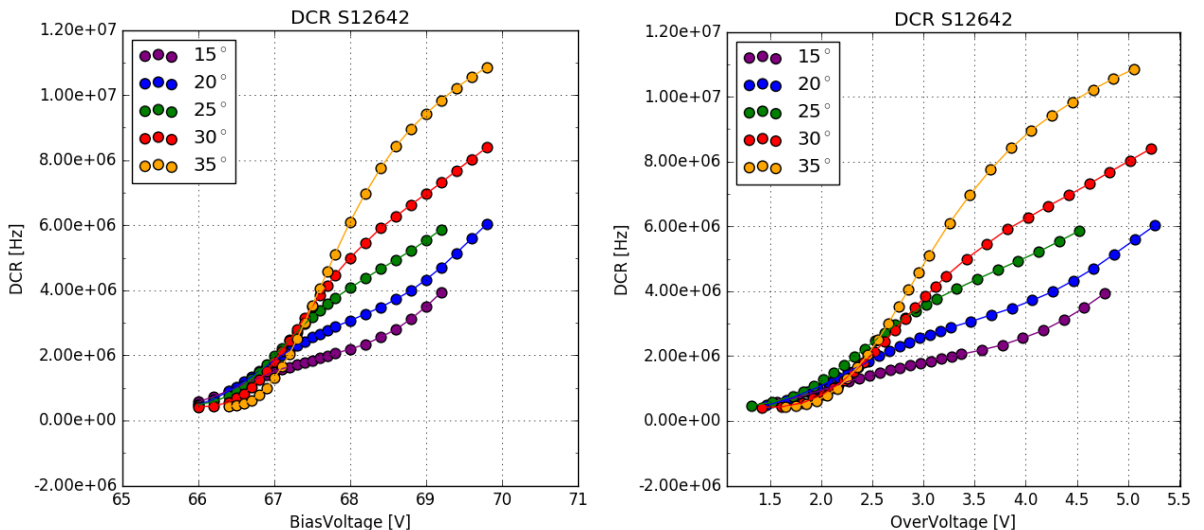


Figure 27: Dark Count Rate of the HPK S12642 pixel, plotted against over-, bias-voltage and temperature.

pulse, due to the high rate of 9-10 MHz. A majority of the pulses overlapping each other and being counted as a 2p.e. event rather than 2 1p.e. events would reduce the Dark Count Rate significantly. At this point, heating of the Silicon Photomultipliers surface due to the high rate could also affect the Dark Count Rate through shifting of the temperature slightly upwards, away from

35° C . So that the Dark Count Rate declared at 35° C is in reality the rate at higher temperatures.

At the lower end of the bias-voltage range, I suspect, that a major part of the found 1p.e. pulses are actually noise related. So the Dark Count Rate changing to a plateau is expected. This is also due to the fact, that my measurements are done with a fixed bias-voltage range. Due to the increase of the breakdown-voltage with rising temperature, part of the measured bias-voltage range corresponding to a very low over-voltage, attributes to this effect. In order to reliably measure beyond an overvoltage of 2.5V in the lower range, the noise would need to be improved.

6.2.3 Optical Cross Talk

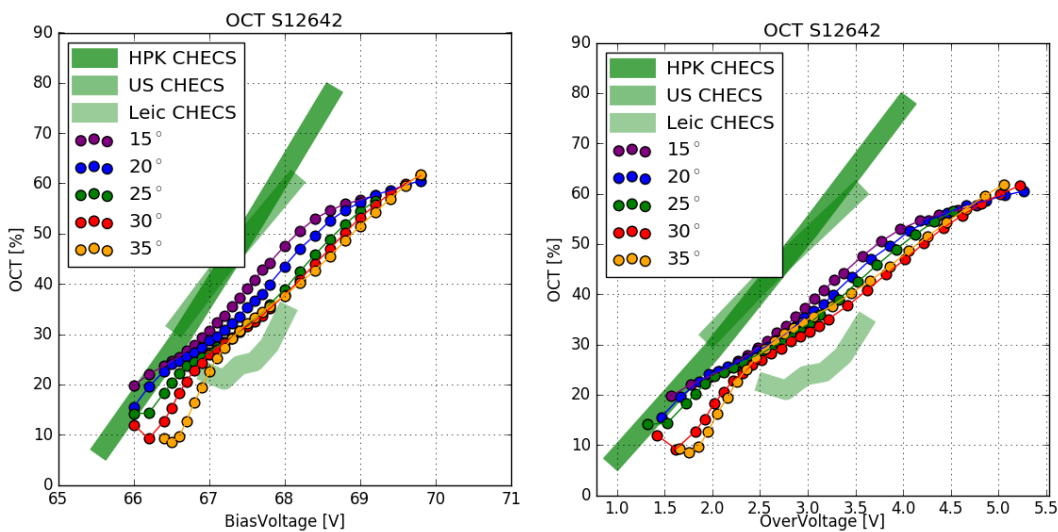


Figure 28: Dark Count Rate of the HPK S12642 pixel, plotted against over-, bias-voltage and temperature.

The Optical Cross Talk should be linear and independent from temperature. This is confirmed for HPK S12642. Minor deviations from that are probably due to slight errors in the breakdown-voltage calculation from the gain regression line. The deviation of 30° C and 35° C below an over-voltage of 2V stems from the way the gain regression line is used to calculate both Dark Count Rate and Optical Cross Talk. At higher temperatures the lower voltage range is dominated by noise, so using the gain regression line to calculate the Optical Cross Talk at those low voltages leads to the visible effect of the first few datapoints of 30° C and 35° C . The deviations between the different groups results at 25° C (green) are caused by 4 major contributions. Firstly the difference in the tested device. While I take measurements on 4 3mm^2 pixels electrically tied together, the way the device will later be implemented into CHEC-S, the groups in the US and Hamamatsu Photonics are likely to run tests on 1 3mm^2 pixel only. Secondly I suspect a slight difference in amplification and shaping electronics. The measurements I conducted as well as the measurements of Leicester are done with the same shaper and buffer

configuration. The difference here is, thirdly, my measurements are done with dark counts only, while measurements from other groups are conducted with a pulsed light source and reading out timed windows. This causes the results from Leicester to be difficult to compare against, their surface temperature of the SiPM is likely much higher than 25° C, and thus, a misinterpreted breakdown-voltage at 25° C causes a shift of the Optical Cross Talk to the right. Lastly the difference in actual data taking and analysis procedure must be mentioned, also this is only of minor concern, as we will see with other measured devices.

6.3 Hamamatsu LCT5 50 μ m 6mm

The Silicon Photomultiplier designated HPK S13360 6050CS fig(29) is an LCT5, meaning Low Cross Talk 5th iteration device from Hamamatsu Photonics. It is one of the most promising candidates for later usage in CHEC-S. It has a pixel size of 6mm² consisting of 14400 cells with a cell size of 50 μ m. The present device and its similar iterations are the first to incorporate trenches bordering each cell, effectively insulating the cells and reducing the prompt Optical Cross Talk very effectively. Tests are done with a single pixel only, in contrast to measurements done on S12642. It is mounted on a ceramic chip and coated with a silicon resin that is UV-transparent. Wire bonds supply the electrical contact. A similar, but not tested, device from the same generation uses through-silicon-via (TSV) technology, realising electrical connection through the silicon bulk, allowing a tighter fit of the cells, with minimal dead-space.

LCT5 6mm

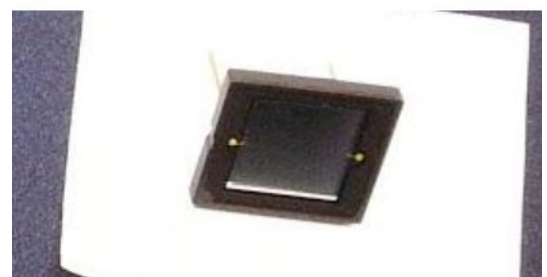


Figure 29: HPK S13360 6050CS pixel

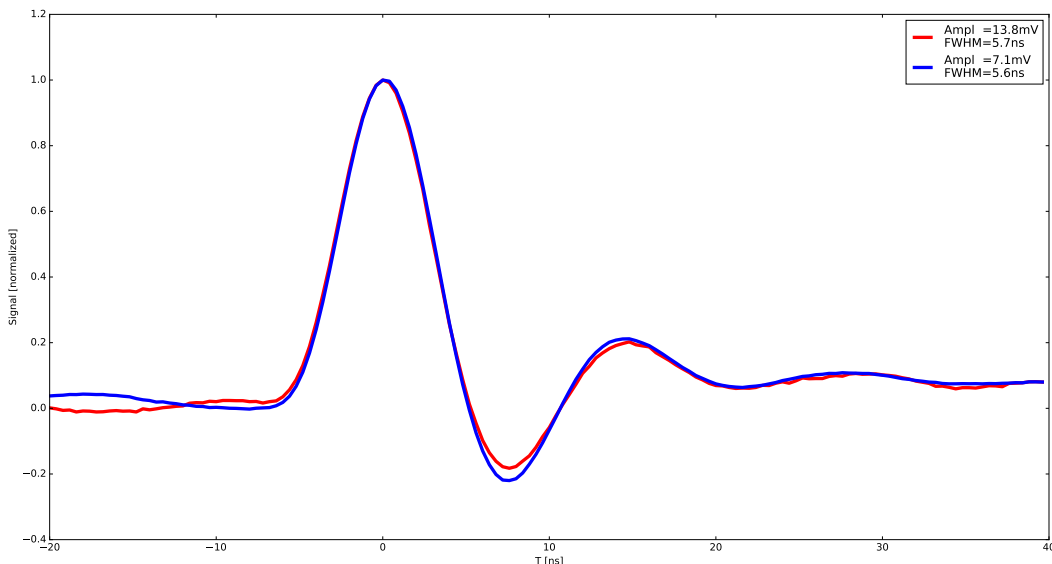


Figure 30: The average pulse shape of the 1 photoelectron in blue and the 2 photoelectron pulse in red of HPK S13360 6050CS at 25° C and at point of operation. Both pulses have a FWHM of around 5ns and ring for approximately 20ns with an undershoot of 20%.

The layout of the single pixel test device made external amplification necessary. I used a MiniCircuits PreAMP, which was supplied with 13V during this test. Shaping of the pulse is conducted by a CHEC-S shaper, modified to fit the new unshaped pulse. The pulse shape fig(30) makes the pulses appear much harder to analyze, due to the possibility of events occurring during

the ringing window. This assumption proved untrue, due to the devices low Dark Count Rate and Optical Cross Talk, so the multi incident probability is also low.

6.3.1 Gain

The gain of the LCT5 50 μ m 6mm device is clearly linear with some minor outliers at 30°C. The same effect as with S12642 is visible at 35°C, again counting noise peaks as 1p.e. peaks, resulting in an apparent lowering of the gain and the slope changing over into a plateau. In Figure(31)(left) the gain is shown, plotted against over-voltage. It is still dependant on temperature, but due to reliable breakdown-voltage calculation, the spread is much smaller than, if plotted against bias-voltage. The same conversion is done to transform relative gain into an absolute gain with sensible units. When parametrized with over-voltage, the gain is essentially temperature independent.

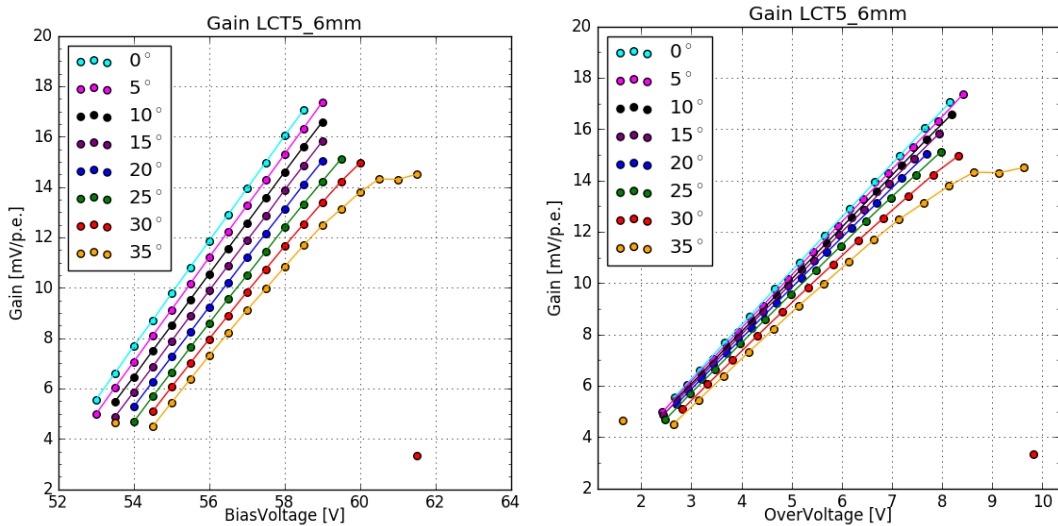


Figure 31: Gain of the HPK S13360 pixel, plotted against over-, bias-voltage and temperature.

6.3.2 Dark Count Rate

The Dark Count Rate of two similar HPK S13360 devices is shown in Figure(32). The bars show the difference between the two devices, the results of one device is used as a reference, while the deviation is illustrated with the filled bar. The Dark Count Rate of HPK S13360 follows the expected behaviour, mostly linear in the significant range and rising with increasing temperature. Below an over-voltage of 2.5V my analysis struggles, I suspect the gain, compared to noise, to be too low for my analysis to pick up pulses. Thus the regression line calculation is unreliable in this range. The turnup at high over-voltages is most prominent at 0°C(teal) after an over-voltage of 9V. This is also the point where the Optical Cross Talk rises very rapidly.

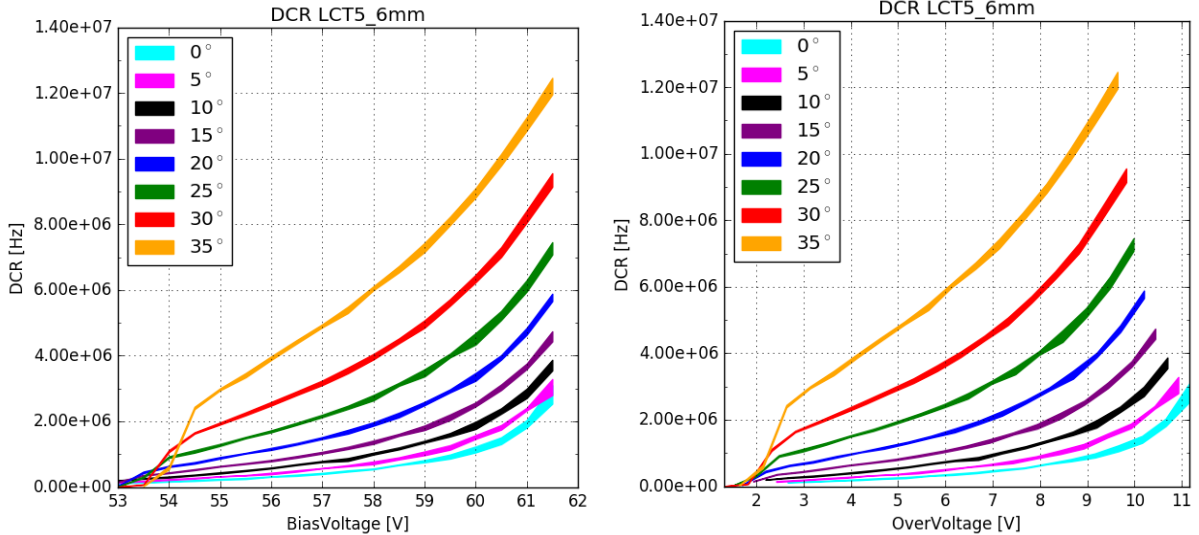


Figure 32: Dark Count Rate of the HPK S13360 pixel, plotted against over-, bias-voltage and temperature.

6.3.3 Optical Cross Talk

Compared to measurements on HPK S13360 done at the Nagoya University, Japan fig(33) (faded green bar), I see a very strong correlation of the Optical Cross Talk in the over-voltage range between 2.5V and 9V. The Optical Cross Talk in this range is linear and independent from temperature, with minor deviations attributed to the breakdown-voltage calculation from the regression line, causing the horizontal shift. In contrast to my technique, using only dark counts, the measurements at Nagoya University followed a pulsed light source approach, reading out a time-window after the laser incident. This could have consequences, since Optical Cross talk with a large delay time could be missed. Deviations below an over-voltage of 2.5V are expected, they are very likely caused by the regression line calculation being unreliable in this range due to the analysis method struggling to pick up pulses using dark counts. Above an over-voltage of 9V, which is also the point of the turnup of the Dark Count Rate, the Optical Cross Talk is no longer linear and the deviation from the results of Nagoya University increase very rapidly. I suspect the rapid increase in both Dark Count Rate and Optical Cross Talk to be caused by the over-voltage reaching ranges, where interpretation of noise as a 1p.e. pulse becomes more likely. This, joint together with the usage of the MiniCircuits amplifier supplied with 13V, makes false interpretation of noise as pulses even more likely. I suspect these two reasons in conjunction are responsible for both, the sudden rise of the Dark Count Rate as well as the deviation of the Optical Cross Talk from linearity and the results of Nagoya University, above over-voltages around 9V. In summary, the correlation between the two measurements, conducted by two different methods of data acquisition and analysis, is evident.

The S13360 series is the first to incorporate physical barriers, called trenches, effectively insulating the cells from each other. This drastically reduces the prompt cross-talk, while increasing the percentage the delayed cross-talk contributes to the overall cross-talk shown. This could also be the reason for the upturn compared to data from the University of Nagoya, at higher over-voltages the contribution from delayed cross-talk is higher. With the trenches effectively reducing the prompt cross-talk and the difference in analysis, the effect could be partially explained by increased contribution of the delayed cross-talk. More on this subject in chapter 7.

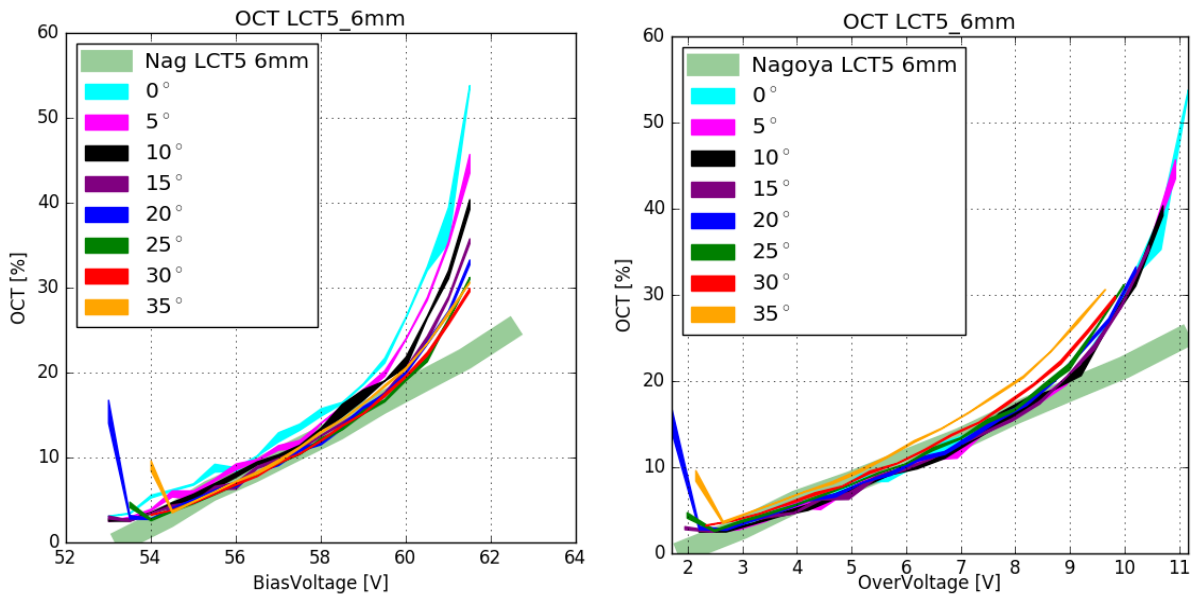


Figure 33: Optical Cross Talk of the HPK S13360 pixel, plotted against over-, bias-voltage and temperature.

6.4 Hamamatsu LCT5 75 μ m 7mm

XXXXXXXXXXXX is a larger LCT5 prototype Silicon Photomultiplier of the same design as S13360-6050CS fig(34). With an increase in cellsize to 75 μ m, the device gains a higher fill-factor than 50 μ m devices. The pixel-area is also expanded to 6.915mm², which will result in a higher fill-factor (less deadspace), so presumably a higher PDE but also a higher OCT. Since it is a prototype device, there is limited data from datasheets. The ID number suggests, that it is also a wire-bond device with a UV-transparent silicon-resin coating. It is also a single pixel test device, so external amplification is necessary with the MiniCircuits PreAMP, supplied with 8V during this test. The signal is also shaped by a differently modified CHEC-S shaper, which results in a pulse shape similar to S12642, but with a much lower amplitude fig(35).

LCT5 7mm



Figure 34: HPK LCT5 7mm pixel

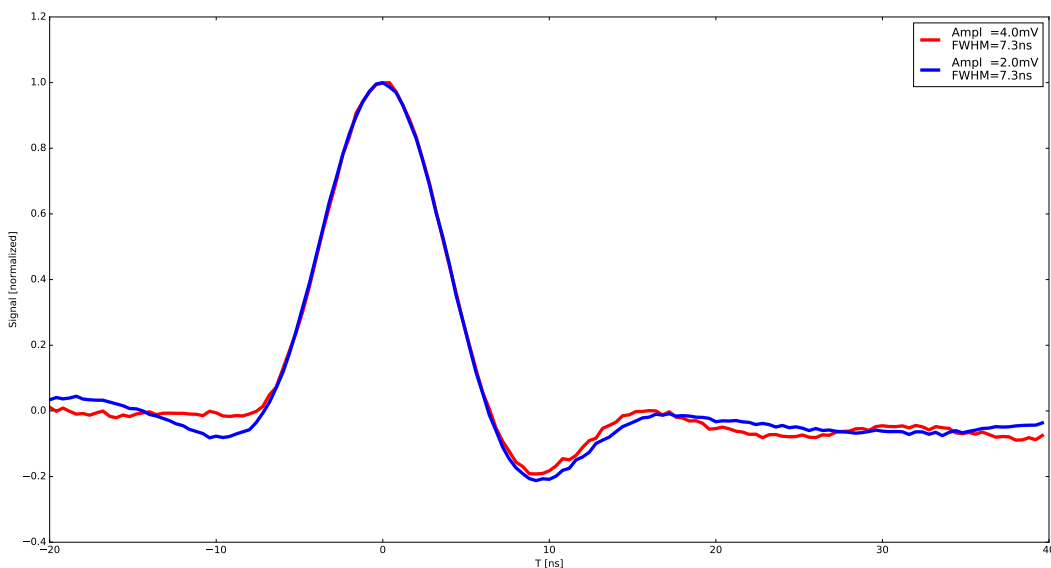


Figure 35: The average pulse shape of the 1 photoelectron in blue and the 2 photoelectron pulse in red of HPK LCT5 7mm at 25° C and at point of operation. Both pulses have a FWHM of around 7ns and an undershoot of 20%, with no ringing.

6.4.1 Gain

Figure(36) shows the gain of the LCT5 7mm device. Two sets of measurements are done for 25°C to extend the measured range. The first set of measurements covers the lower over-voltage range, where the low gain makes external amplification necessary with a MiniCircuits PreAMP supplied with 8V. I chose the lowest possible amplification of the PreAMP, so that reaching the point of saturation of the oscilloscope input is as late as possible as the over-voltage rises. Saturation of the oscilloscope occurs due to the possibility of generating very large p.e. (>10 p.e.) events at the higher over-voltages, which are saturating the input. Joint together, the LCT5 7mm device and the MiniCircuits PreAMP at 8V reach this point at an over-voltage of ~ 6 V. In Figure(36) the results from

the lower range measurement are displayed as the lower-range green line extending between an over-voltage of 1.6V to 5.4V. The configuration for the second test removes the PreAMP from the setup, which makes the lower over-voltage range unaccesible, but extends the range to higher over-voltages. This configuration reaches the point of saturation at an over-voltage of ~ 8 V. The higher range measurement results are displayed as the second green line (25°C) extending from 3.4V to 7.2V over-voltage in Figure(36). There is a clearly visible overlap of the two measurements between ~ 3.4 V and ~ 5.4 V . It also seems, that the gain dependency on temperature is reversed. While for all other devices, the gain lowers with rising temperatures, the LCT5 7mm device seems to show inversed behaviour. This inverse behaviour is caused by the calculation of the breakdown-voltage from the gain-regression line, with this and the bias-voltage, the over-voltage is calculated, causing a horizontal shift. Plotting the gain versus bias-voltage, however, shows the expected behaviour.

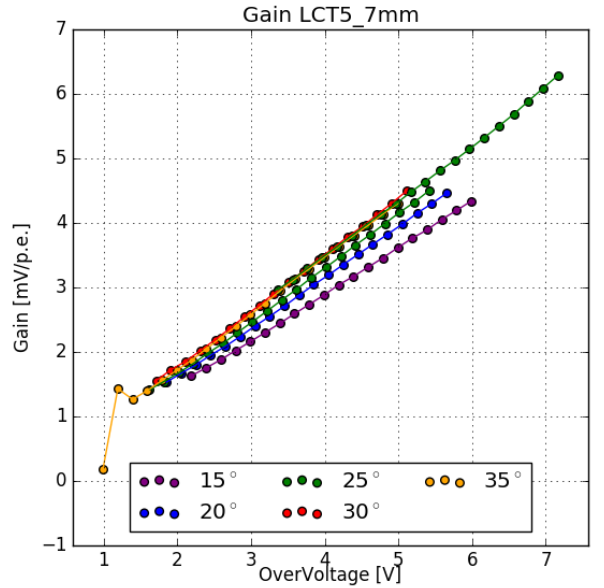


Figure 36: Gain of the HPK LCT5 7mm pixel

6.4.2 Dark Count Rate

The behaviour of the Dark Count Rate of the HPK LCT5 7mm device is shown in Figure(37) and is as expected, in contrast to the behaviour of the gain of LCT5 7mm, as discussed in section 6.4.1. It follows a linear progression in the relevant range and increases with rising temperature. I suspect the over-voltage range above $\sim 2.5V$ to be relevant. The extended range measurement at $25^{\circ}C$ confirms this behaviour. LCT5 7mm shows a linear Dark Count Rate over an over-voltage range of 4V. The faded green bar in Figure(37) shows results from measurements undertaken by the Department of Physics and Astronomy at the University of Catania. Those measurements were conducted on the exact same device, which is an important point, but with a different method of data acquisition and data analysis. Analysis techniques are discussed in chapter 7. The correlation between the two experiments is evident, although there is differences in the acquisition and analysis process. This is further proof for the relevancy of the analysis technique employed in this paper.

6.4.3 Optical Cross Talk

The Optical Cross Talk is expected to be linear and independent from temperature. This is the case in the, in section 6.4.2 established, relevant over-voltage range of above $\sim 2.5V$. Minor deviations are attributed to the calculation of the breakdown-voltage from the gain-regression line. The over-voltage is calculated from the former and the supplied bias-voltage, which in turn causes a slight horizontal shift. With that, comparing my results to the measurements from the University of Catania shows a strong correlation. Keeping in mind, that the process of data acquisition and analysis is different for both measurements further proofs the analysis technique valid.

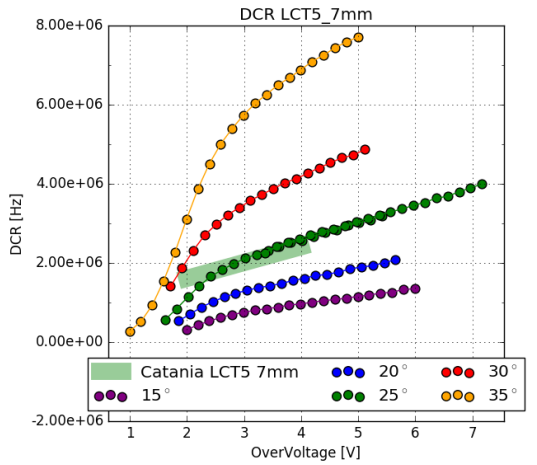


Figure 37: Dark Count Rate of the HPK LCT5 7mm pixel

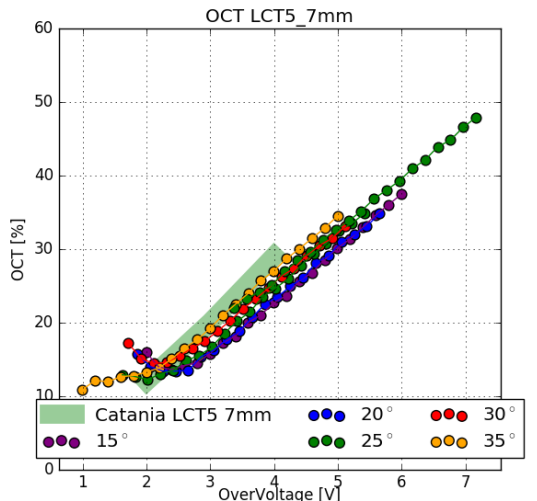


Figure 38: Dark Count Rate of the HPK LCT5 7mm pixel

6.5 Hamamatsu LVR 50 μ m 6mm

The Silicon Photomultiplier by Hamamatsu Photonics with the designation 6050HWB-LVR-LCT is a special prototype of the LCT5 design. LVR is an abbreviation of Low Voltage Range, meaning the device is meant to be operated at much lower operation voltages than other LCT5 devices. It has the same physical size as an LCT5 50 μ m 6mm device (S13360 chapter ??), a pixelsize of 6mm pixel with a cellsize of 50 μ m. The recommended point of operation however is \sim 15V below that of the S13360 device, specifically at 40.2V(LVR) instead of 54.7V (S13360). The unshaped signal is similar to other LCT5 devices, therefore using the same modified CHEC-S shaper is feasible in this case, resulting in a similar pulse shape fig(40). After that the signal is amplified with the same MiniCircuits PreAMP supplied with 8.5V.

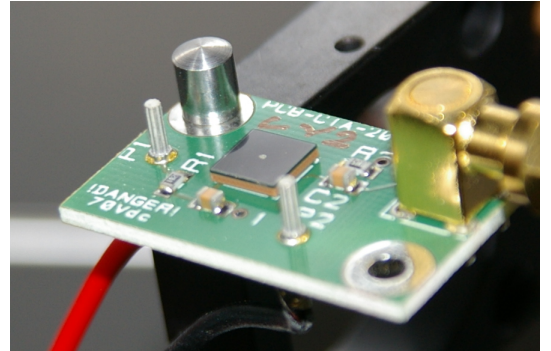


Figure 39: HPK LVR 6mm pixel

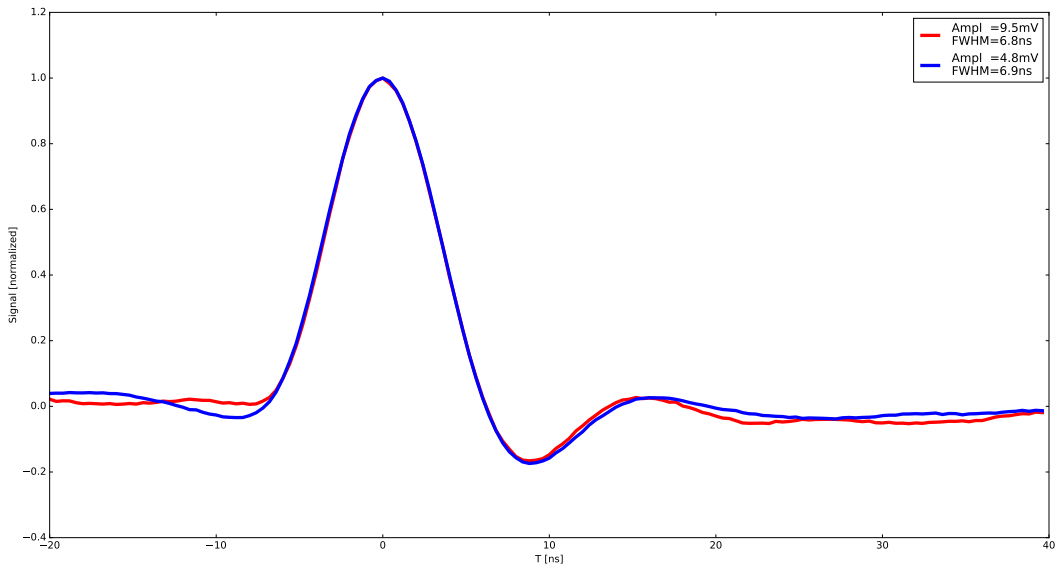


Figure 40: The average pulse shape of the 1photoelectron in blue and the 2photoelectron pulse in red of HPK LVR 6mm at 25° C and at point of operation. Both pulses have a FWHM of around 7ns and an undershoot of 20%, with no ringing.

6.5.1 Gain

Figure(41)(right) shows the gain of the LVR 6mm device. It is, as expected, linear over a long range and nearly independent of temperature when parametrized with over-voltage. The flattening of the slope to a plateau shape in the lower over-voltage range, is caused by the

analysis being unable to identify peaks lower than the set threshold. Only taking into account the linear region, limits the range, where the results are relevant to an over-voltage range of ~ 2.5 V. Saturation of the oscilloscope in this range is not visible, but a check with a more expanded range revealed, that the point of saturation of the oscilloscope is at an over-voltage of ~ 5 V. The apparent overlap of the gain, when plotted against over-voltage, is based on the calculation of the breakdown-voltage being very reliable due to the large linear range. Plotted versus bias-voltage fig(41)(left) the expected behaviour of the gain, lowering with increasing temperature, is visible.

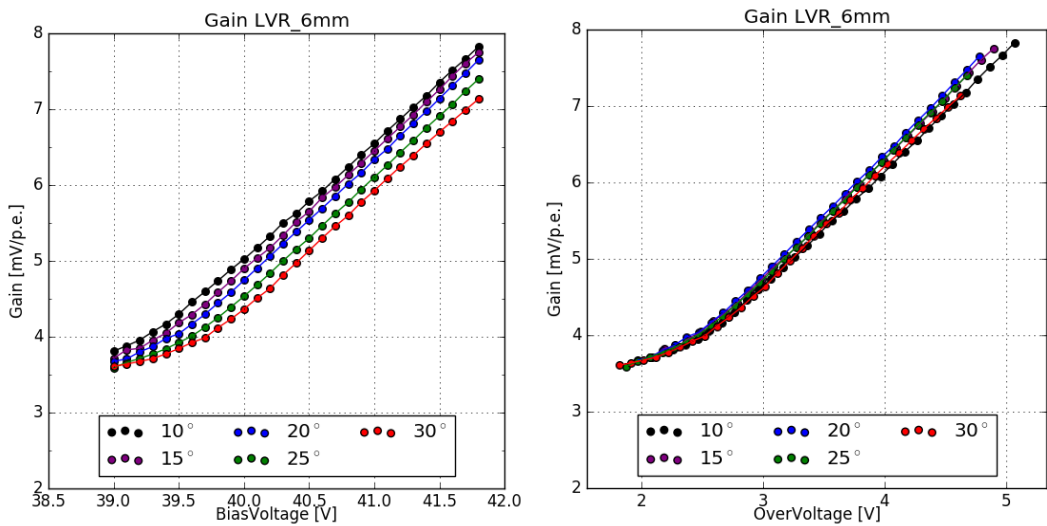


Figure 41: Gain of the HPK LVR 6mm pixel

6.5.2 Dark Count Rate and Optical Cross Talk

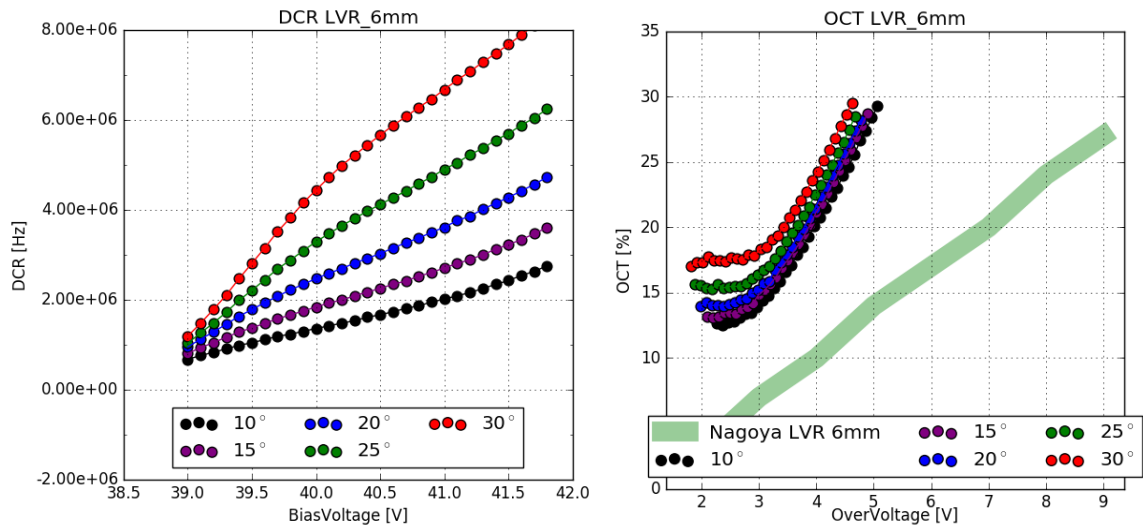


Figure 42: Dark Count Rate and Optical Cross Talk of the HPK LVR 6mm pixel

The Dark Count Rate fig(42)(left), taking into account only the relevant over-voltage range of $>\sim 2.5V$ seems to correlate, while the resulting Optical Cross Talk fig(42)(right) is very high compared to results from the University of Nagoya, which also cover a much wider range. Only taking into account the previously established relevant over-voltage range of $>\sim 2.5V$, the resulting Optical Cross Talk is a factor of 2 higher. This uncertainty is a contrast to results from previous devices, where strong correlations between different groups and measurement techniques are evident. I suspect, that the device examined by me and the device present at Nagoya University are slightly different prototypes.

6.6 SensL FJ60035 6mm 35 μ m

The Silicon Photomultiplier by SensL with the designation FJ-60035 is also a candidate device for use in CHEC-S. It is also a 6mm device, but with a much smaller cellsize of 35 μ m, using the TSV technology, so there are no wire-bonds present. This results in 22292 cells on a single pixel with a fill-factor of 75% . It is coated with plain glass. The recommended point of operation is around 30V bias-voltage, lower even than that of the HPK IVR prototypes. The device is, by the manufacturer, pre-mounted on a printed circuit board, called a test array. This test array contains a fast output, that directly couples to the cells, and a slow output, conventionally read out via the quench resistor. For the conducted tests, I used the fast output amplified with the MiniCircuits PreAMP supplied with 12V. The SensL device was the first device measured, therefore the analysis procedure used was an older iteration compared to the procedure for the Hamamatsu devices.

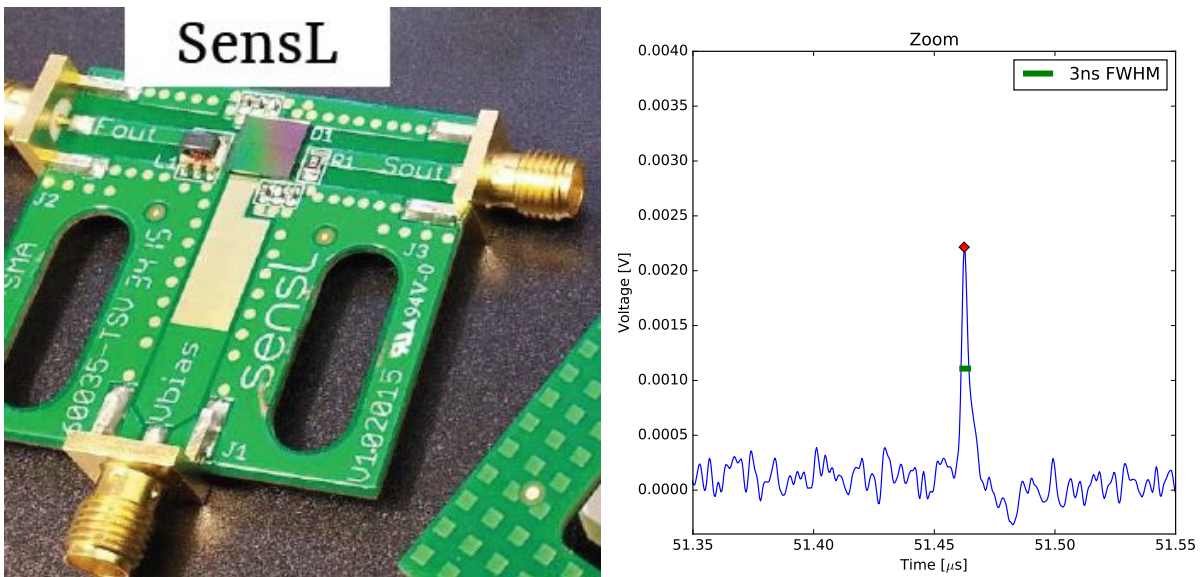


Figure 43: SensL Test Array and pulse shape at bias-voltage = 29V0

6.6.1 Gain

Evaluating the SensL pulse area spectra shows the 1 p.e. position and Δ p.e. overlapping, so using the older analysis iteration introduced no error when evaluating the gain of the SensL device. It is clearly linear over a wide temperature range from -5°C to 35°C over an over-voltage ranging from 2V up to 8V. When plotted versus over-voltage the spread of the gain is even tighter signaling slight temperature independency, but still following the expected behaviour of decreasing with increasing temperature.

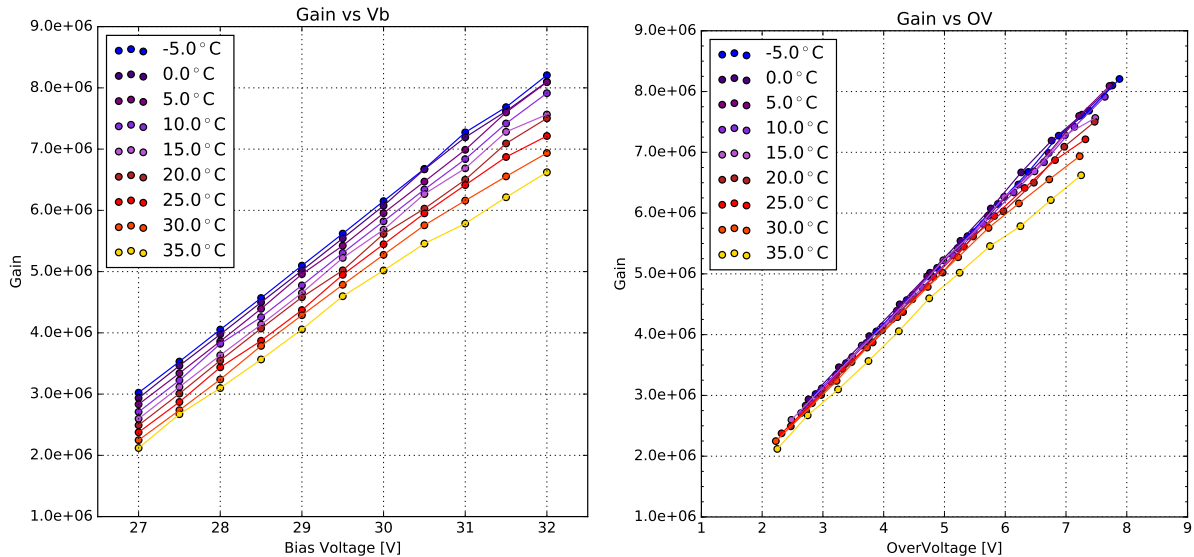


Figure 44: Gain of the SensL FJ-60035 test array

6.6.2 Dark Count Rate and Optical Cross Talk

The Dark Count Rate fig(45)(left) also shows the expected behaviour. At very low temperatures the changes in rate over the over-voltage range is minimal. Increasing the temperature shows a rapid increase in thermally induced dark counts. The Optical Cross Talk fig(45)(right) on the other hand is independent of the device temperature, also as expected.

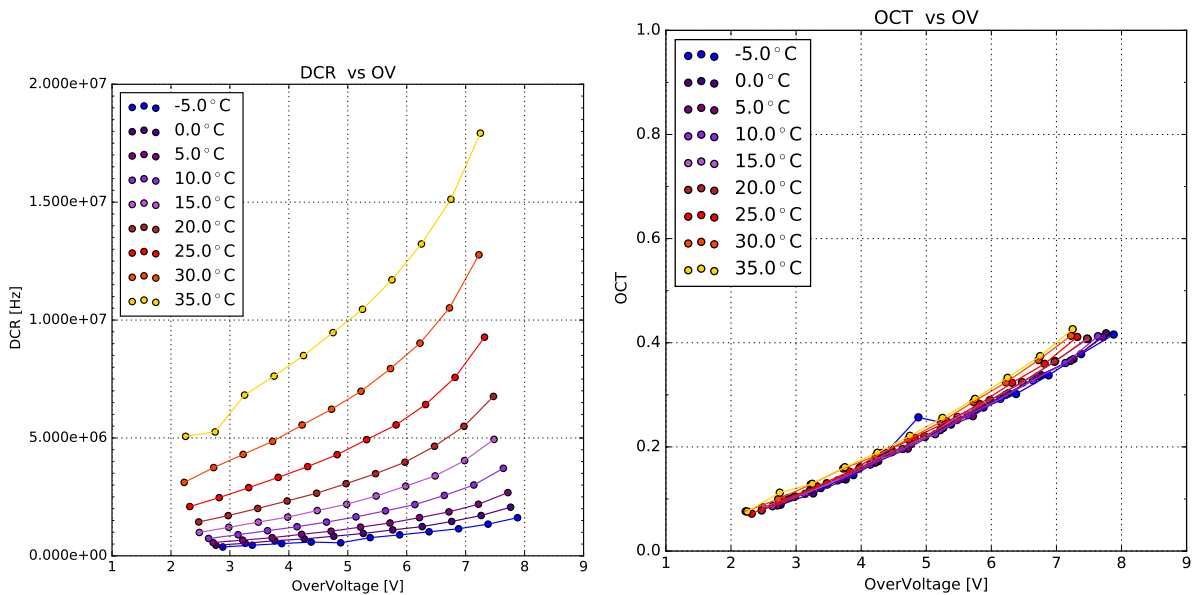


Figure 45: Dark Count Rate and Optical Cross Talk of the SensL FJ-60035 test array

7 Comparison

A comparison of the performance of all devices is the significant step for choosing the Silicon Photomultiplier later to be used in CHEC-S. In order to do this, all measured characteristics are compared versus over-voltage. Operation of the CHEC-S camera in GCT will come down to a decision between two operational points. The first point will be marked by an Optical Cross Talk of under 15%. Every other attribute of the Silicon Photomultiplier at this over-voltage is then compared. This point will trade off precision for efficiency, a lower Optical Cross Talk makes real event detection easier, on the other hand, a lower Photon Detection Efficiency may forfeit a lot of potential data.

The second point of operation is marked at the highest achievable Photon Detection Efficiency. My conducted measurements do not involve this, other groups are comissioned to determine the point of highest Photon Detection Efficiency, in other conducted measurements, that are comparable 48. This point will assure the highest detection of event photons, but will trade that for an increase in detector noise, due to the higher Dark Count Rate and more importantly Optical Cross Talk.

Comparing results to other groups is shown in Figure (46), using different experimental setups and procedures and therefore also entirely different analysis techniques. Comparing against results from the University of Leicester, the University of Nagoya and the University of Catania, all of which are conducting fixed window readout of the SiPM after an expected light-pulse from a flasher-LED or pulsed laser.

7.1 Dark Count Rate

Comparing the Dark Count Rate of the measured devices and results from the other groups is shown in Figure 46. The differences in analysis procedure will only have a slight impact on the presumed Dark Count Rate, since all experiments record dark-count events over their respective acquisition time windows. On the other hand, if the readout window is sufficiently small, events originating from afterpulsing or delayed crosstalk could be missed. All groups experience the same multi-hit coincidence, meaning a light-event or dark-event coinciding with another, forming a (partial)multi p.e. event.

Only two of the 5 measured device have measurements results from other groups to compare, as it is not their focus. In the case of both, the LVR 6mm and the LCT5 7mm results can be discussed to some degree as matching. While the correlation is obvious for the LCT5 7mm device Figure(??)(red), where the covered measurement range in this paper exceeds the external results, while matching and showing the same trend, the LVR 6mm results deviate. Between an over-voltage of 3V and 4V the results overlap, the trend on the other hand is obviously different. Additionally the limit on the higher range due to noise makes it impossible to compare against

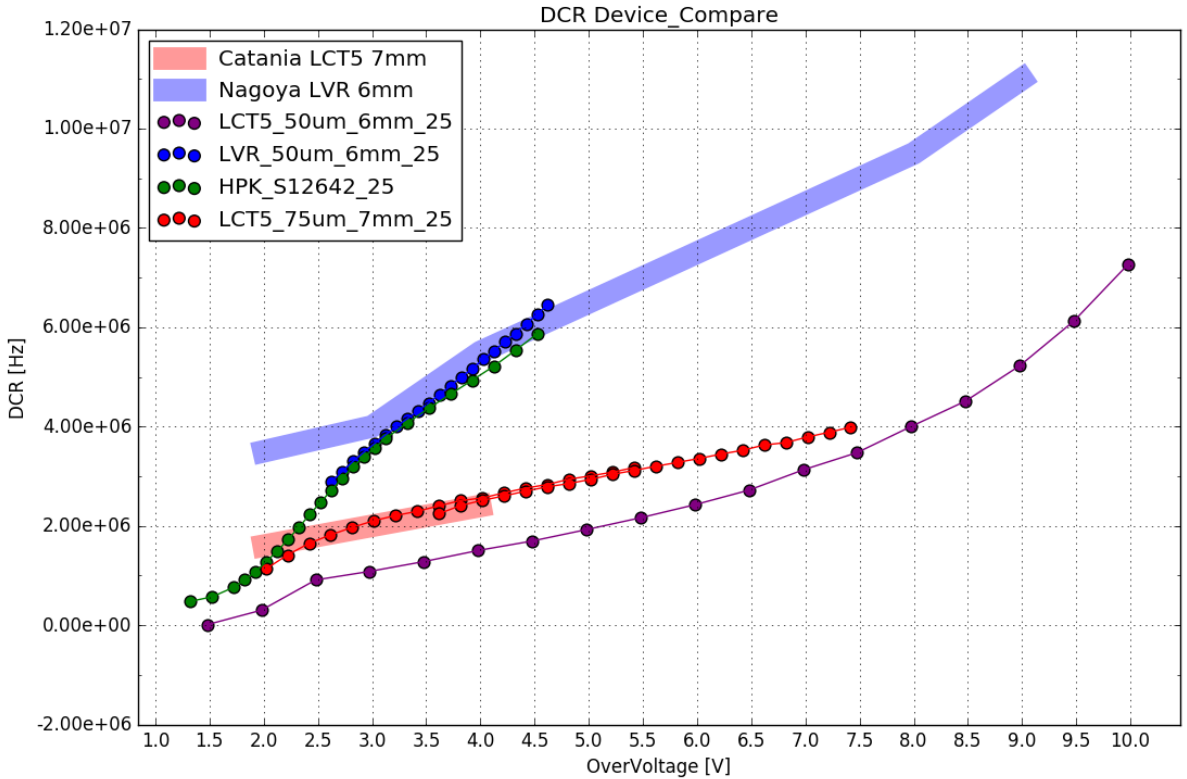


Figure 46: Dark Count Rate comparison of measured devices at 25°C. Description

the full range measured by the external group, so the DCR for LVR 6mm must be labeled as not matching.

7.2 Optical Cross Talk

The comparison of the Optical Cross Talk between the different groups and the results presented in this paper are dependant of the analysis and acquisition procedure. Extended trace analysis, utilized in this paper captures all aspects of the Optical Cross Talk, prompt and delayed as well as afterpulsing. The procedure of time window analysis, utilized by the groups being compared to, are, due to their limited window, either biased towards the prompt cross talk or in extreme cases, will not be able to capture delayed cross talk or time-delayed afterpulsing at all. Comparing data analysis techniques, for example, at the University of Leicester is therefore a vital step. Their approach utilizes a pulsed laser as light source and involves no cooling of the SiPM tile. The waveforms are extracted from the scope and a small time window is defined from the known time position window of the incident pulse to search for peaks, find their value and generate a histogram. To the pulse area histogram, a theoretical model of contributing factors is fitted. This theoretical model simulates characteristics, updating continuously to find their correct values. Those values are the full set of characteristics of the device in testing, among them: gain curve, breakdown-voltage, OCT, PDE, noise, dynamic range, crosstalk probability.

There are a number of differences in their approach compared to the one utilized in this paper,

most important is the time window size. If the window after an incident pulse is too short, data loss is a possibility, depending on the delay time of delayed cross-talk and afterpulsing assisted by traps with long lifetimes. This is a problem, especially with devices of the LCT5 generation implementing physical trenches isolating the cells and effectively reducing the prompt cross-talk, the contribution from the prompt cross-talk to the overall Optical Cross Talk is lowered. For time window analysis with short window times, missing data from delayed cross-talk and afterpulsing, because it will not be recorded yet, would lead to errors in the overall Optical Cross Talk results being lower than expected.

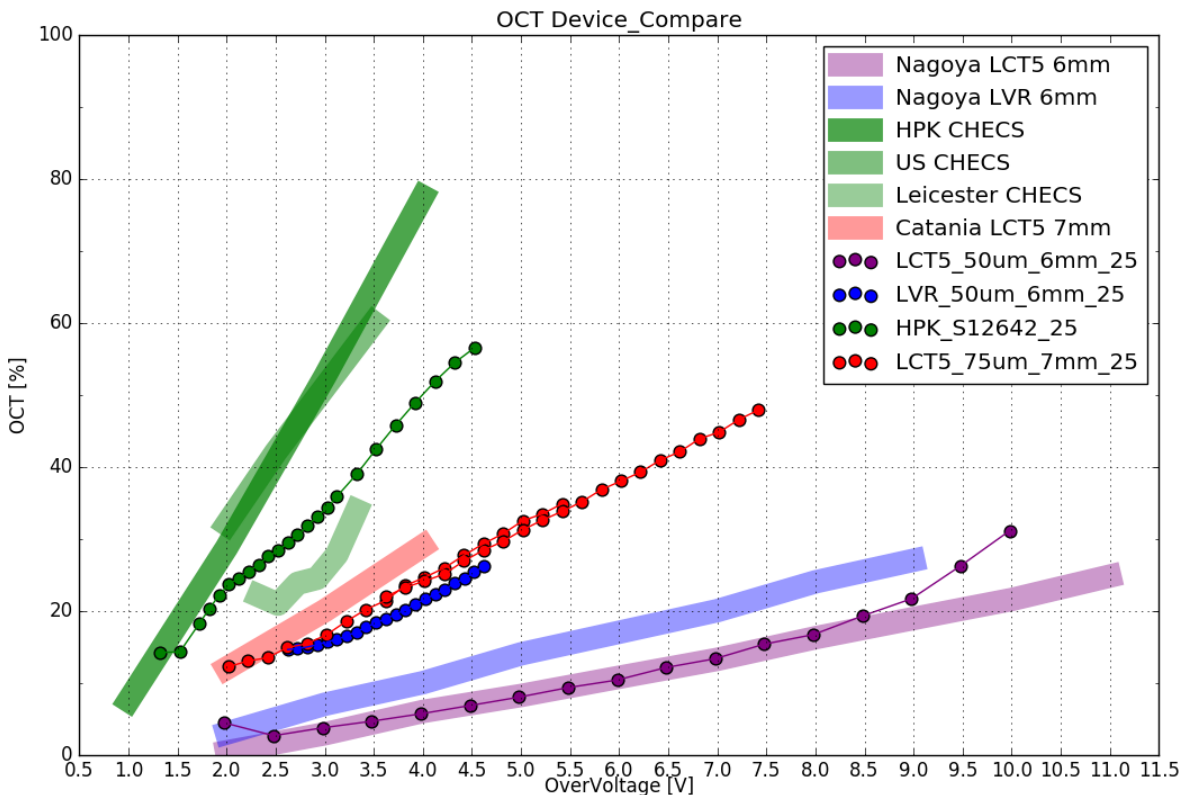


Figure 47: Cross Talk comparison of measured devices at 25°C. Description

This is indeed the case for the S12642 tile in Figure 47 (green). The light green bar below the dotted data presented in this paper shows the results form the University of Leicester indeed being lower. In purple results of the LCT5 S13360 device with physical trenches are shown. Compared to results from the University of Nagoya, there is a prominent upturn at around an over-voltage of $\sim 8V$. This could be due to the differences in analysis technique. The University of Nagoya also employs time window analysis. LCT5 posseses lowered prompt cross-talk probability, so the contribution of delayed cross-talk to the overall cross-talk is higher than for S12642. With rising over-voltage the ratio between prompt and delayed cross talk shifts towards a higher contribution from delayed cross-talk. While at lower over-voltages ($\sim 2V$) contributions are mostly equal, at high over-voltages ($\sim 8V$) the contribution of delayed cross-talk is expected

to be above 80%, probably due to higher penetration depth and avalanche probability. Results of the LCT5 7mm device from both groups mostly overlap, the slight shift between them is most likely caused by a small error in the breakdown-voltage calculation, due to no cooling of the tile in experiments involving light. In addition, the slope of both results seems to be mostly equal, and the extended range measurement, overlapping with the low-range results confirms that.

Even though results from 3 different groups mostly correlate, or are at least partially understood differences, the Optical Cross Talk of LVR 6mm Figure 47 (blue) compared to the results from the University of Nagoya do not show any correlation at all. This is concerning, because comparing S13360 (purple) to the same group showed strong correlation over a wide over-voltage range. Since there is also no datasheet present yet, this device is a prototype, I can only assume, that the device I examined is physically different than the device present at Nagoya. It may just be a difference in coating, which combined with the TSV technology could lead to the present uncorrelation. (quote confidential HPK talk)

7.3 Photon Detection Efficiency

Since the measurement technique in this paper utilizes only dark counts and aims at giving an understanding of the Optical Cross Talk and temperature dependency of the different SiPMs proposed, no PDE measurements are possible. The point of operation with the highest PDE is determined by a different group in Japan, at the University of Nagoya. Figure (48) shows the current results of their endeavors. The usual procedure of comparing SiPMs is done on a plot of PDE vs OCT. This gives the most insight of the capabilities of the different devices compared to the two proposed operating points chapter(7). Taking the PDE ascertained by the group at Nagoya and comparing it to the resulting Optical Cross Talk from this paper produces Figure(not yet done).

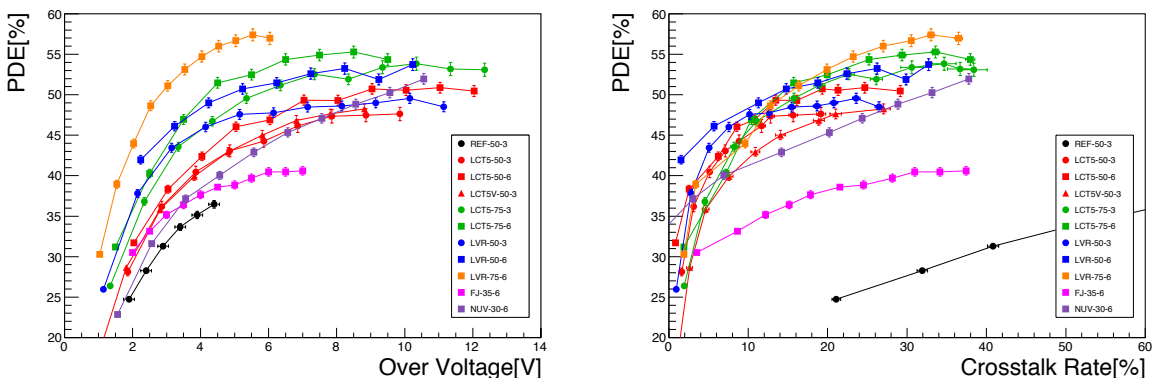


Figure 48: Photon Detection Efficiency Comparison Plots from the University of Nagoya

Plotting PDE versus OCT is the standard way to compare the viability of different SiPMs, it gives a correlated overview of the two most significant characteristics. Comparing all devices at

the two proposed points of operation produces the table in Figure(49). This table together with Figure (not yet done) of the 5 measured devices in this thesis is used to confirm results between groups and assist in the decision on the most viable SiPM for CHEC-S. The final decision will be taken by the group at the University of Nagoya, by Hiro Tajima, the Photosensor work group lead scientist? of GCT based on measurements on substantially more devices ref prelim. nagoya table .

7.4 Point of Operation Comparison

Device	Min. OCT			Max. PDE		
	OCT	DCR	PDE	OCT	DCR	PDE
CHECS	15%	0.5 MHz	25% (DS)	50%	5 MHz	48% (DS)
LCT5 6mm	15%	3.4 MHz	49% (Nagoya)	22%	5 MHz	51% (Nagoya)
LCT5 7mm	15%	2.0 MHz	42% (Catania)	25%	2.5 MHz	53% (Catania)
LVR 6mm	15%	2.5 MHz	43% (Nagoya)	>27%	>6MHz	>50% (Nagoya)
SensL	15%	3.0 MHz	37% (Nagoya)	30%	6 MHz	40% (Nagoya)

Figure 49: Comparison table of the measured devices in the style of the 2 proposed operation points for CHEC-S. First point represents minimal achievable OCT, second point represents maximum achievable PDE. PDE values taken from results of other groups. Note that the LCT5 6mm device can achieve even lower OCT value ($\sim 3\%$ at $V_{ov} = 2.5$)

8 further analysis

8.1 Dark Count Rate recalibration with multi incident probability

With increasing Dark Count Rate the probability of two dark events happening at the same time rises with increasing bias-voltage. Taking for example the Dark Count Rate of S13360 and taking the FWHM of the characteristic pulse we can calculate the probability for every dark rate at every bias-voltage and can extract a probability curve. Wouldnt that just make the DCR rise even higher since 1 2p.e. are now 2 1p.e.s' ??

8.2 Prompt and delayed cross talk ratio

What happens if we take the OCT of S13360 and scale it with an expected prompt to delayed crosstalk ratio. evidence only from confidential HPK talk, need citations. Could just make new plots in HD, evaluate.

9 Conclusion and Outlook

Hmhmm

For that purpose 5 different SiPM from two manufacturers have been examined.

10 Glossary

1. SiPM - Silicon Photomultiplier
2. IACT
3. CTA - Cherenkov Telescope Array
4. LST
5. MST
6. SST
7. GCT
8. CHEC
9. HPK - Hamamatsu Photonics K.K.
10. SensL - Sense Light

11 Bibliography

References

- [1] Jim Hinton et al. Teraelectronvolt Astronomy Ann. Rev. Astron. Astrophys., 47:523
- [2] Julien Rousselle et al. Construction of a Schwarzschild-Couder telescope as a candidate for the Cherenkov Telescope Array: status of the optical system
- [3] Design Concepts for the Cherenkov Telescope Array CTA, An Advanced Facility for Ground-Based High-Energy Gamma-Ray Astronomy ; arXiv:1008.3703v3 [astro-ph.IM] 11 Apr 2012
- [4] Teresa Montaruli et al. The small size telescope projects for the Cherenkov Telescope Array
- [5] The ASTRONET Infrastructure Roadmap ISBN: 978-3-923524-63-1
- [6] Jim Hinton et. al Seeing the High-Energy Universe with the Cherenkov Telescope Array Astroparticle Physics 43 (2013) 1-356
- [7] John Murphy SensL J-Series Silicon Photomultipliers for High-Performance Timing in Nuclear Medicine
- [8] A. N. Otte et al. Characterization of three high efficient and blue sensitive Silicon photomultipliers
- [9] http://astro.desy.de/gamma_astronomy/cta/index_eng.html
- [10] <http://www.ung.si/en/research/laboratory-for-astroparticle-physics/projects/cta/>
- [11] Photosensor Characterization for the Cherenkov Telescope Array: Silicon Photomultiplier versus Multi-Anode Photomultiplier Tube ; arXiv:1308.1390v1 [astro-ph.IM] 6 Aug 2013
- [12] J. Rosado S. Hidalgo Characterization and modeling of crosstalk and afterpulsing in Hamamatsu silicon photomultipliers. arXiv:1509.02286v2 [physics.ins-det] 21 Oct 2015
- [13] Benjamin Glauß. Optical Test Stand and SiPM characteriation studies. MasterâŽs Thesis, RWTH Aachen University, June 2012.

12 Appendix

A CTA

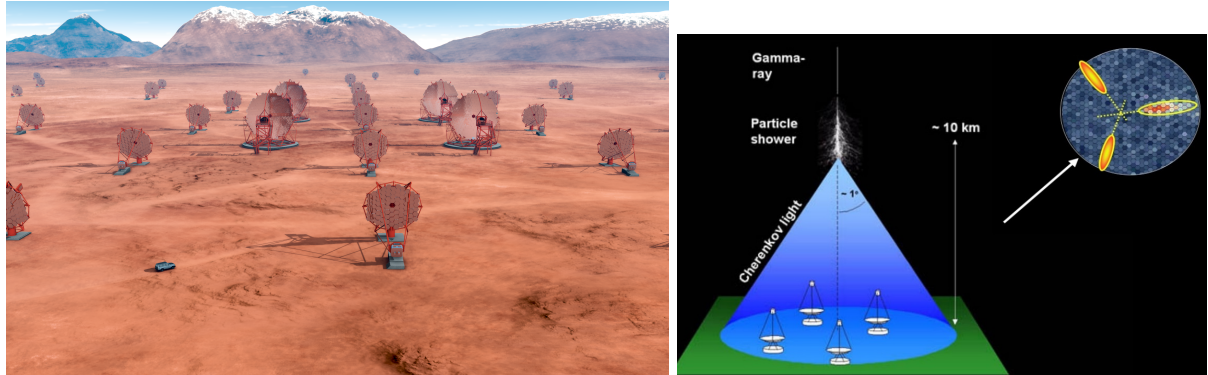


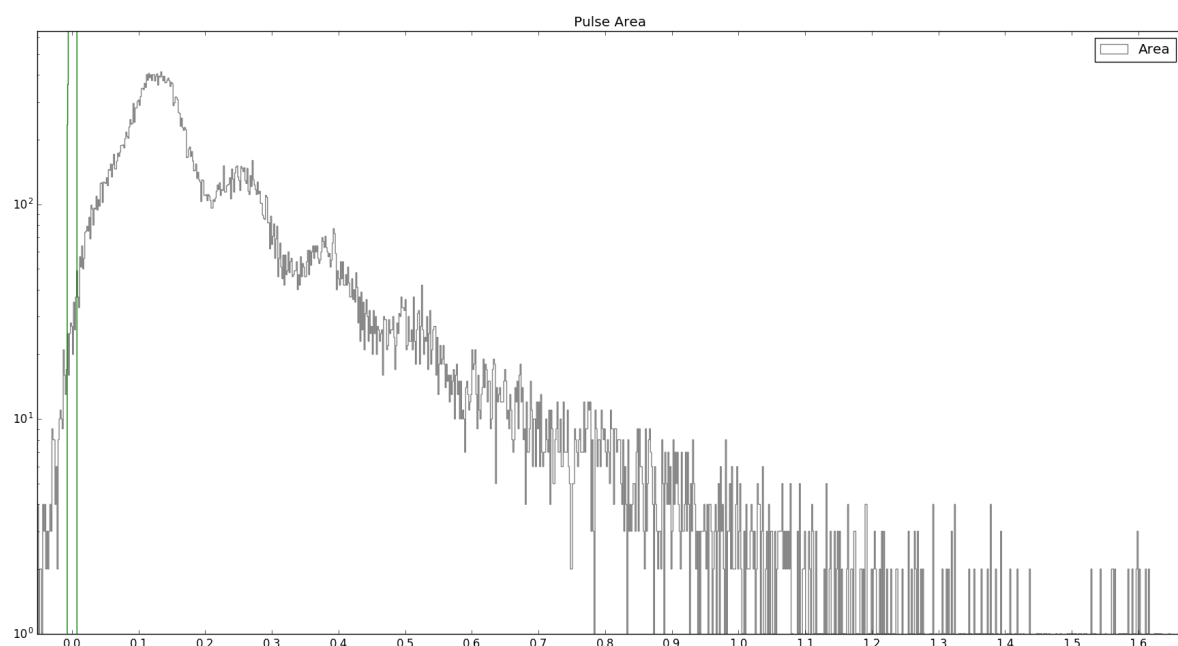
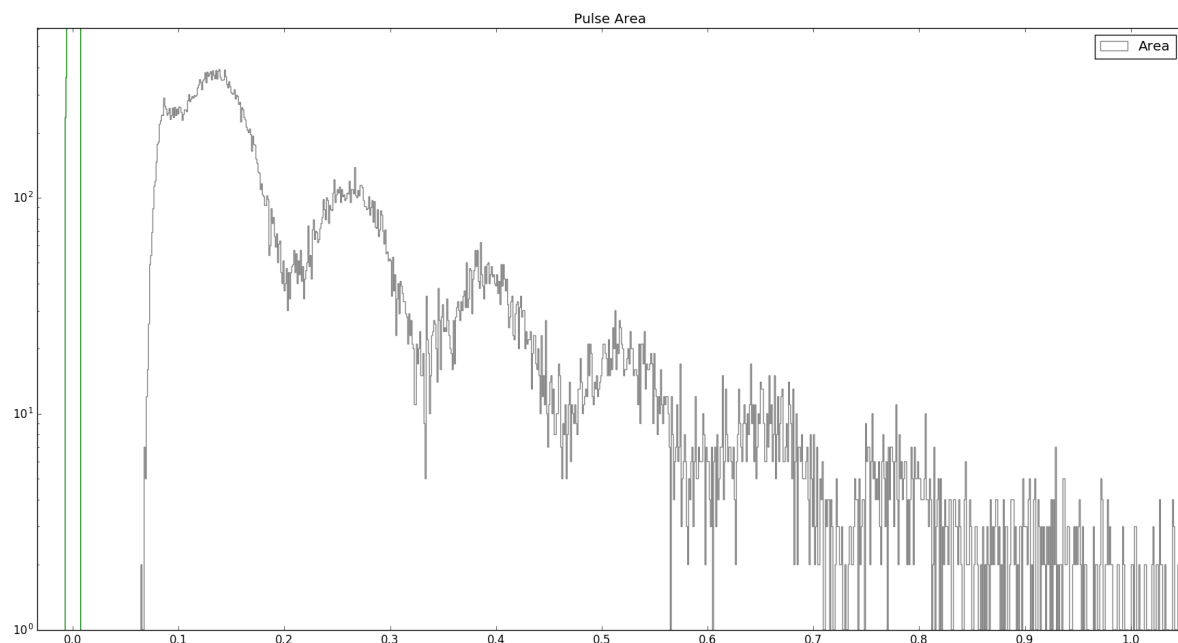
Figure 50: A render of the finished CTA Array at the site in Namibia (left) with visible LSTs and MSTs, and the Shower Path Reconstruction technique of the stereoscopic view employed by current IACT experiments like HESS, MAGIC, VERITAS (right).

B progenitor experiments of CTA



Figure 51: IACT Projects: HESS in the Khomas Highland, Namibia. MAGIC at the Roque de los Muchachos Observatory on La Palma , one of the Canary Islands. VERITAS at Mount Hopkins, Arizona, USA

C Pulse Area Spectra of different integration window widths



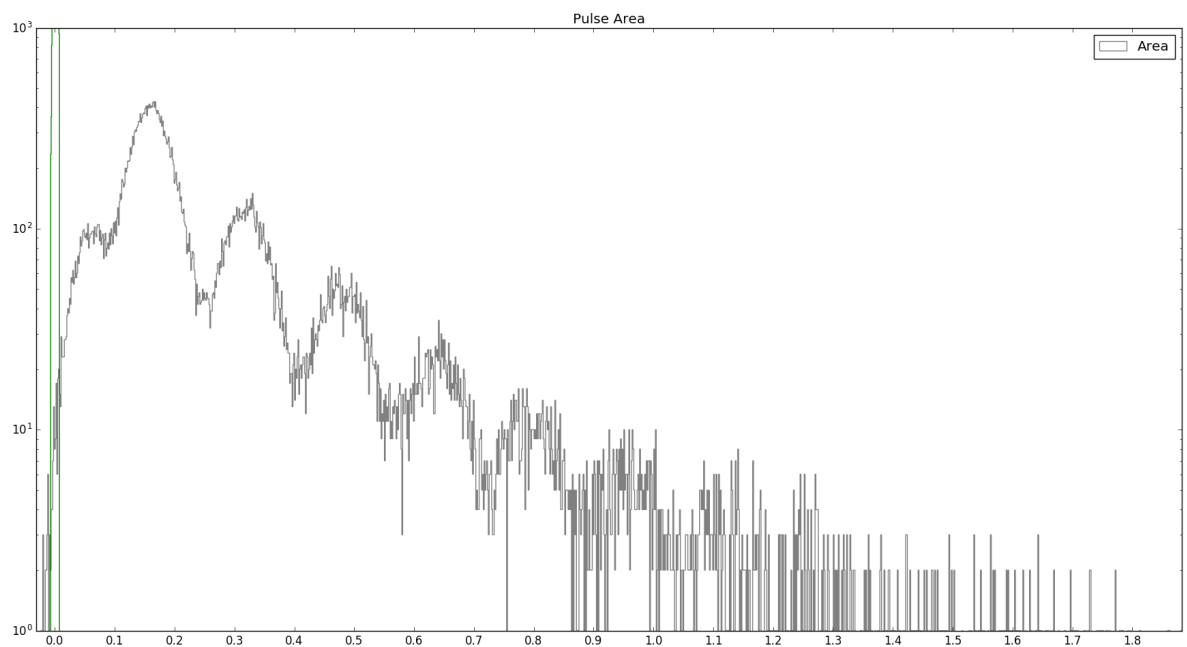


Figure 52: Pulse Area Spectra with window widths of 5 left 5 right (top), 5 left 20 right (middle), 10 left 10 right (bottom) bins respectively. Left of the 1p.e. peak of the top picture a part of the 0p.e. peak is visible. The middle figure shows the distortion an asymmetrical integration window causes. The bottom figure is the employed integration window to derive the pulse area histogram.

D BreakdownVoltage

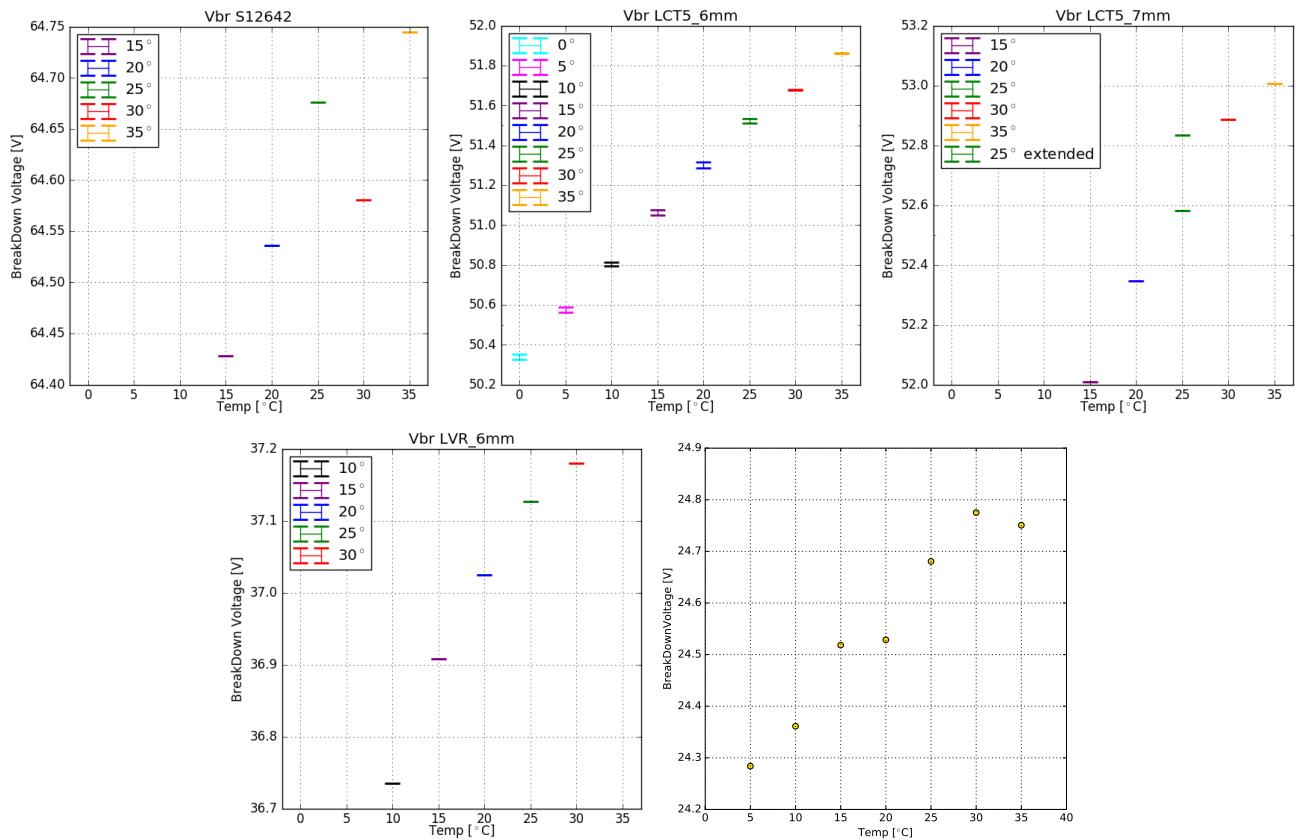


Figure 53: Dependency of the breakdown-voltage of temperature for the 5 measured devices.

For LCT5 7mm , the extended range measurement adds an extra datapoint at 25°C
 HPK S12642 (CHEC-S) (top left) ; HPK LCT5 6mm (top middle) ; HPK LCT5 7mm (top right) ; HPK LCT5 LVR 6mm (bottom left) ; SensL FJ60035 (bottom right).

Device	$\Delta V / T$ [mV/°C]
CHECS	13.1 ± 4.1
LCT5 6mm	43.5 ± 0.4
LCT5 7mm	53.0 ± 4.0
LVR 6mm	25.6 ± 2.6
SensL	15.0 ± 1.1

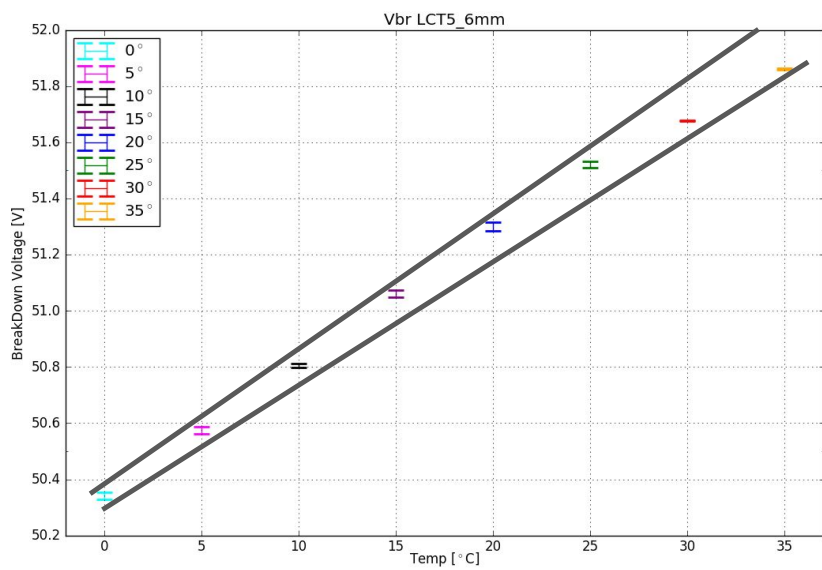


Figure 54: The extracted breakdown-voltage dependence of all measured devices, derived from two regression lines and their mean. For some devices the breakdown-voltage dependency is known through datasheet values. S12642 = , S13360 = , SensL FJ60035 =

E Pulse Area and Height Spectra

Example pulse area spectra

F CHEC-S pixel comparison

Comparison of results from 10 different pixels on the CHEC-S (HPK S12642-1616PA-50) array. Every pixel is analyzed with the same technique and analysis parameters.

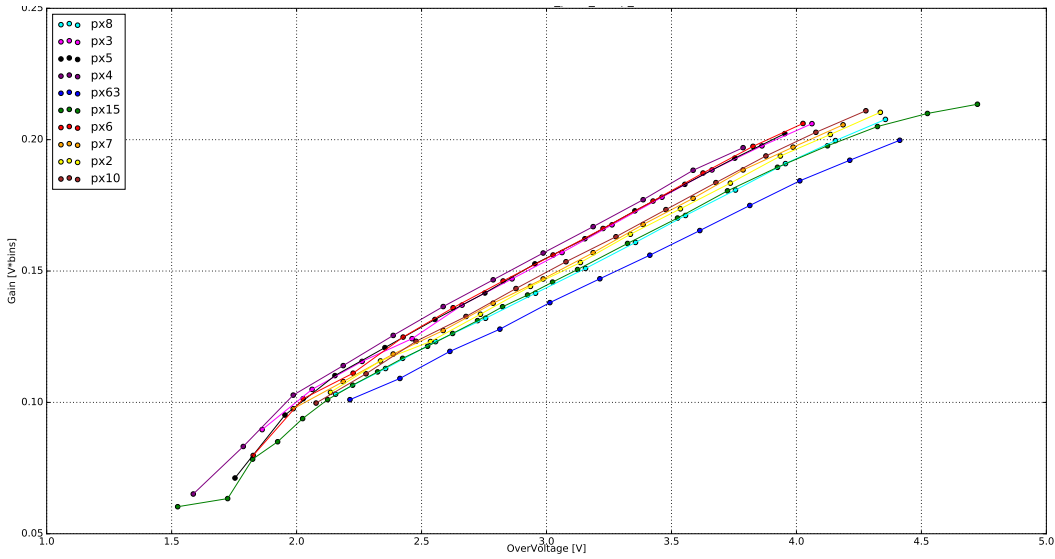


Figure 55: Gain comparison of 10 different pixels of the CHEC-S (HPK S12642-1616PA-50) array

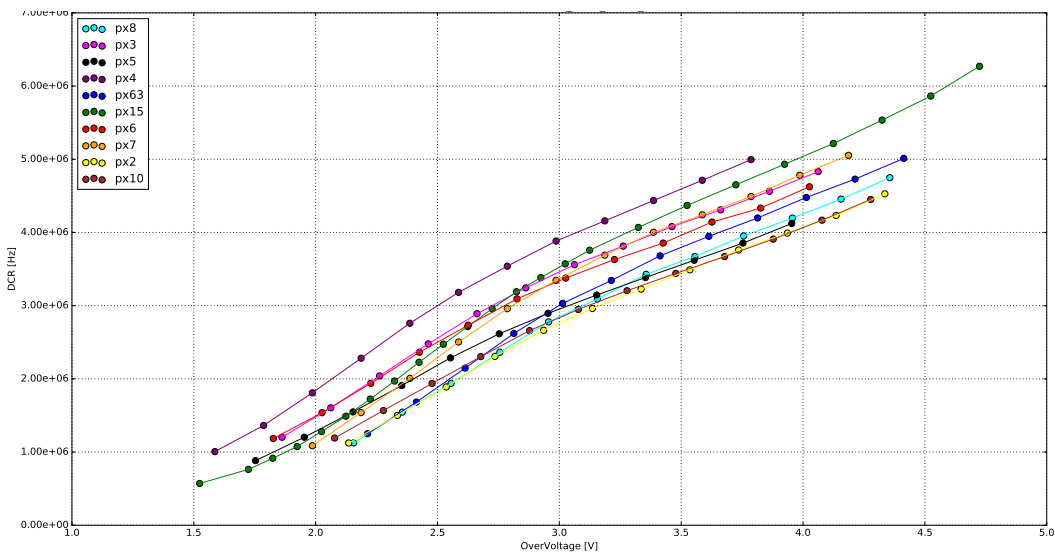


Figure 56: DCR comparison of 10 different pixels of the CHEC-S (HPK S12642-1616PA-50) array

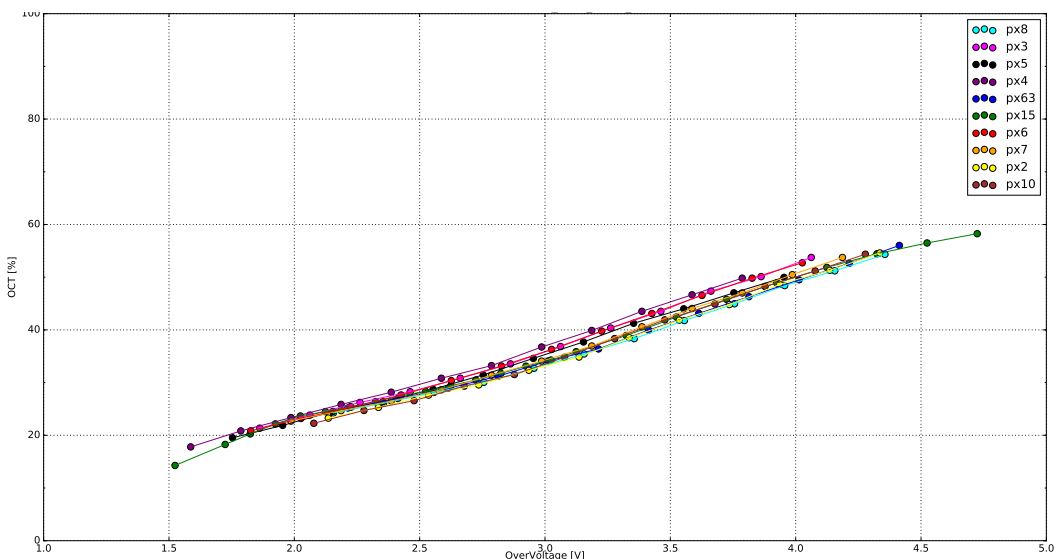


Figure 57: OCT comparison of 10 different pixels of the CHEC-S (HPK S12642-1616PA-50) array

G Additional Data Analysis Plots

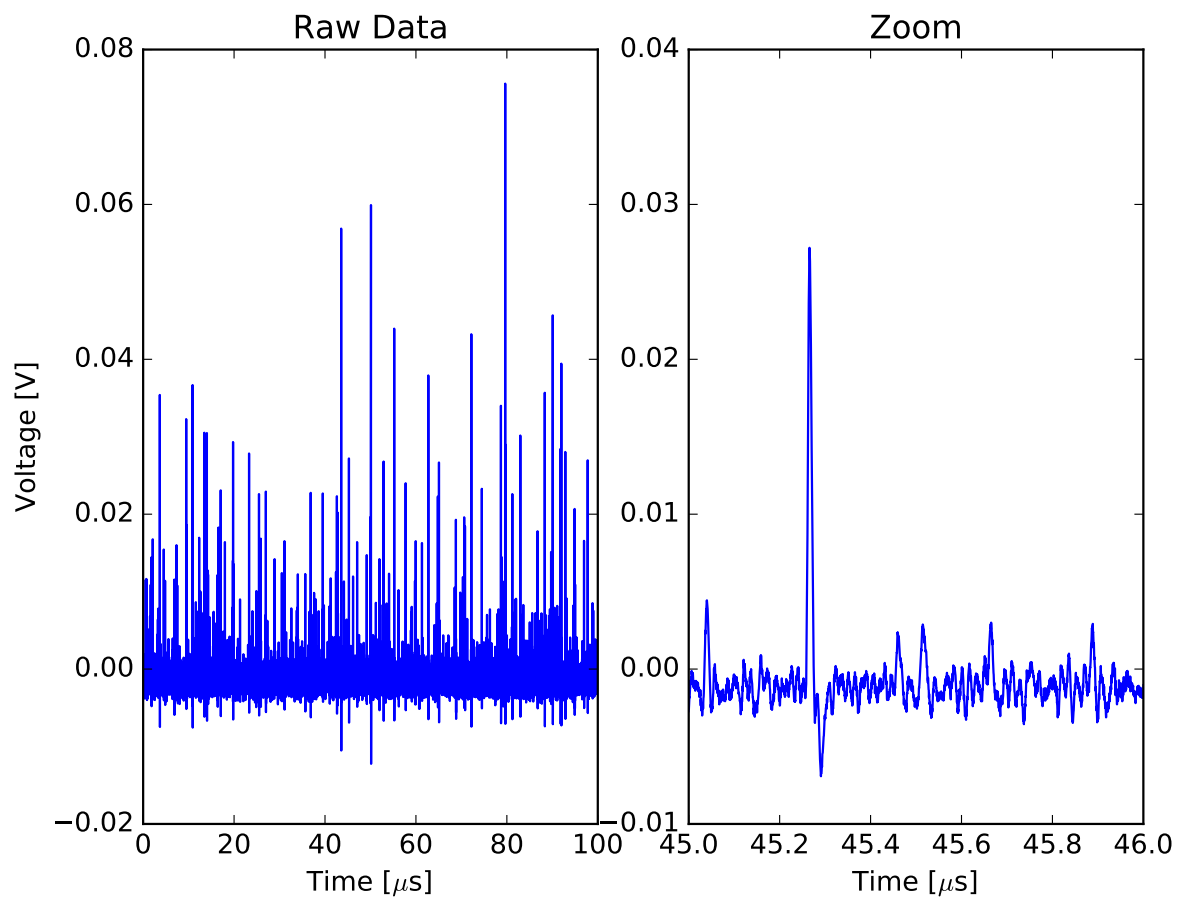


Figure 58: Description

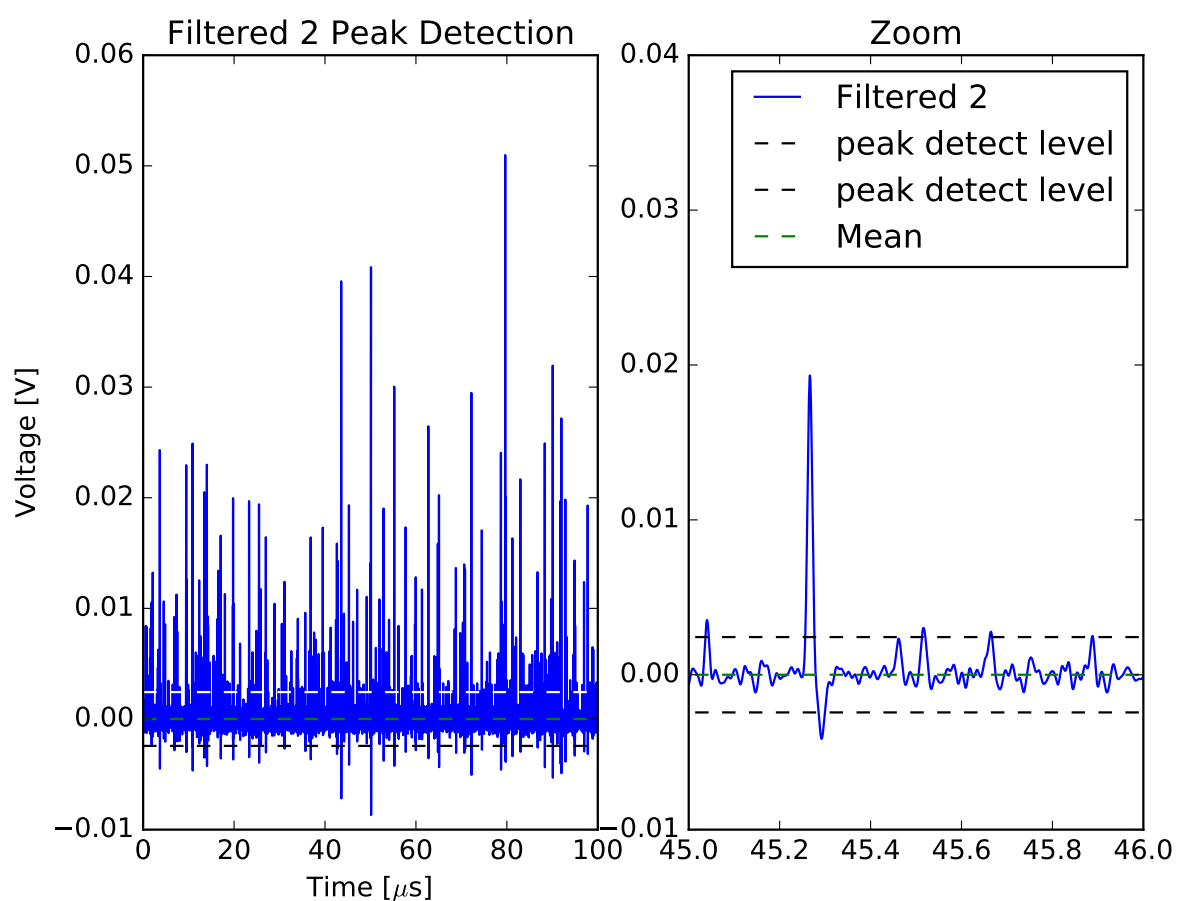


Figure 59: Description

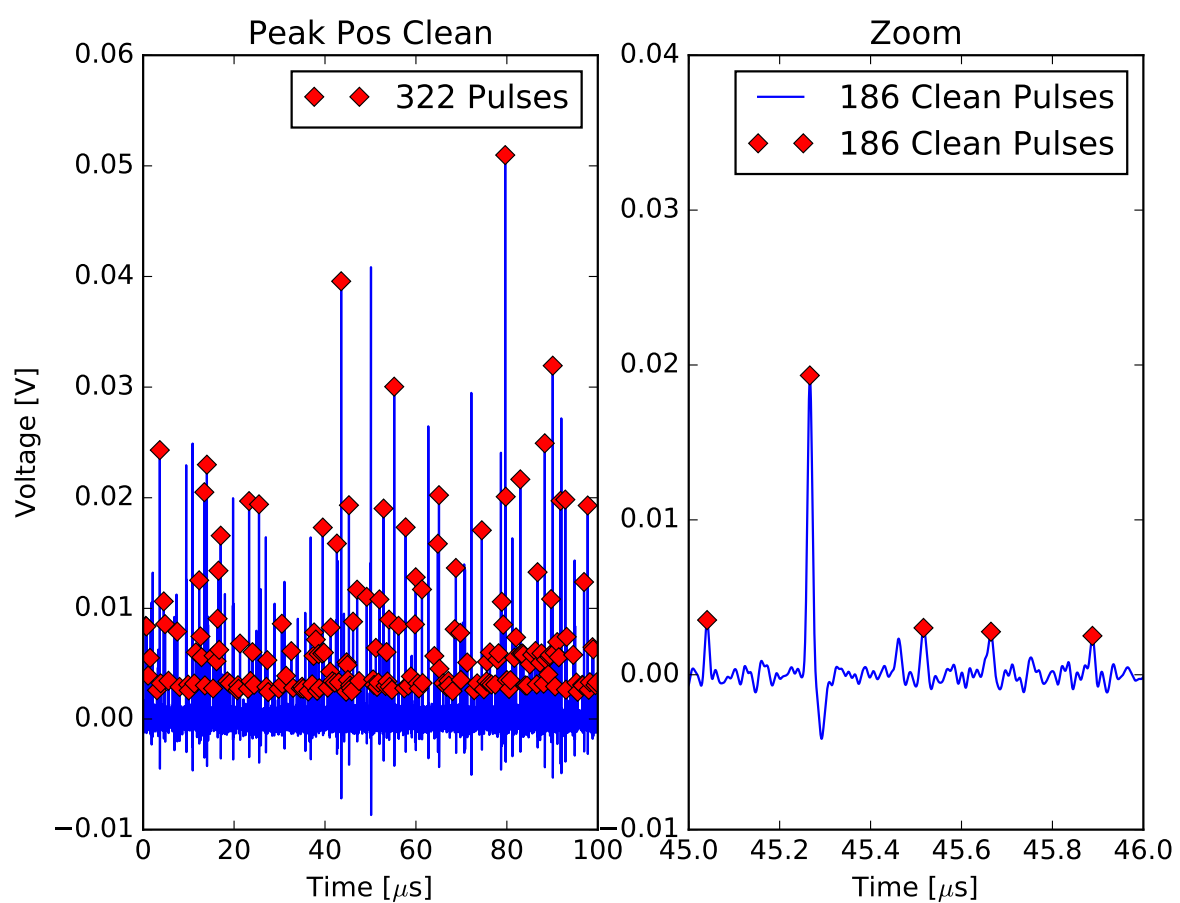


Figure 60: Description

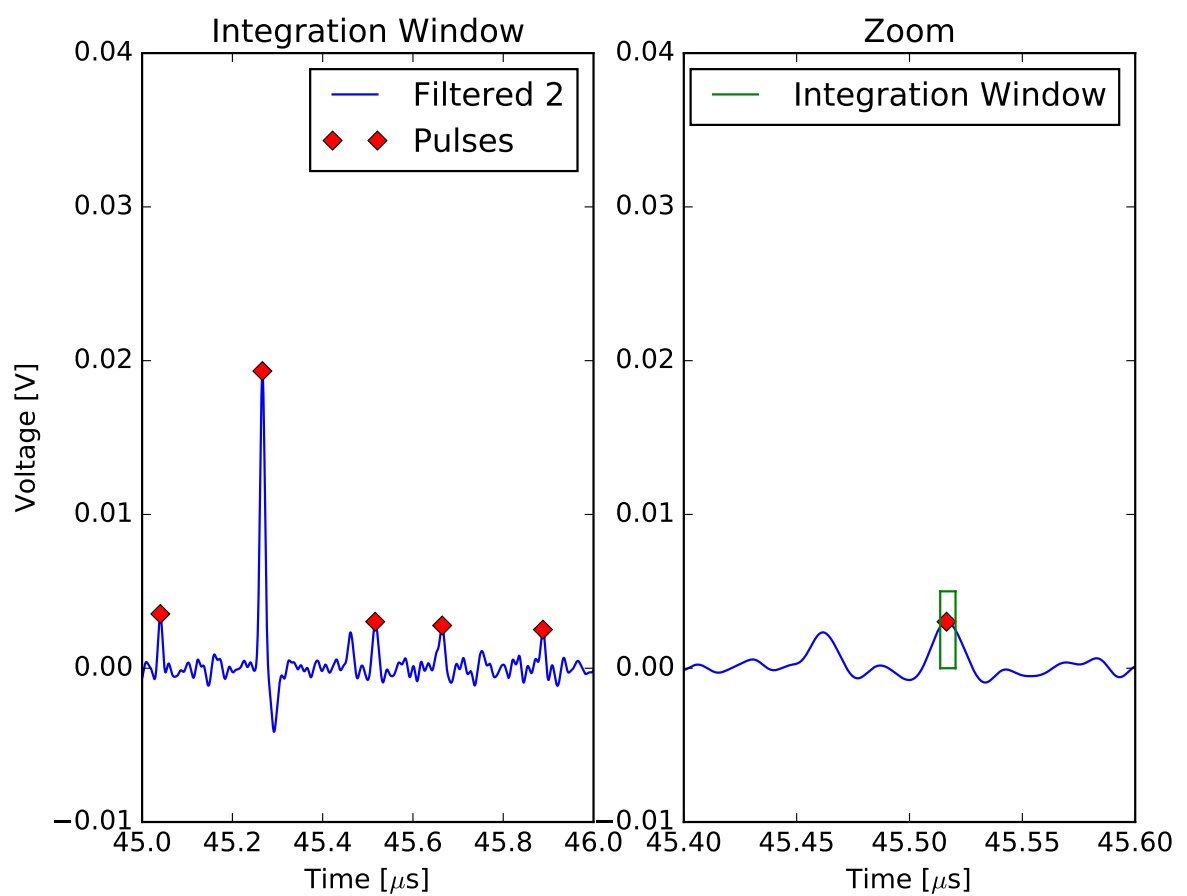


Figure 61: Description

Erklärung zur Master-Thesis

Hiermit versichere ich, die vorliegende Master-Thesis ohne Hilfe Dritter nur mit den angegebenen Quellen und Hilfsmitteln angefertigt zu haben. Alle Stellen, die aus Quellen entnommen wurden, sind als solche kenntlich gemacht. Diese Arbeit hat in gleicher oder ähnlicher Form noch keiner Prüfungsbehörde vorgelegen.

Darmstadt, den April 17, 2017

(B. Gebhardt)